


Cite this: *RSC Adv.*, 2022, 12, 5466

# Silver cluster doped graphyne (GY) with outstanding non-linear optical properties†

Saba Zahid,<sup>a</sup> Alvina Rasool,<sup>a</sup> Ali Raza Ayub,<sup>a</sup> Khurshid Ayub,<sup>b</sup> Javed Iqbal,<sup>b</sup> M. S. Al-Buriahi,<sup>d</sup> Norah Alwadai<sup>e</sup> and H. H. Somaily<sup>fg</sup>

This research study addresses the computational simulations of optical and nonlinear optical (NLO) characteristics of silver (Ag) cluster doped graphyne (GY) complexes. By precisely following DFT and TD-DFT hypothetical computations, in-depth characterization of  $\text{GY@Ag}_{\text{center}}$ ,  $\text{GY@Ag}_{\text{side}}$ ,  $\text{GY@2Ag}_{\text{perpendicular}}$ ,  $\text{GY@2Ag}_{\text{above}}$ , and  $\text{GY@3Ag}_{\text{center}}$  is accomplished using CAM-B3LYP/LANL2DZ while the CAM-B3LYP/mixed basis set is used for study of  $2\text{GY@Ag}_{\text{center}}$ ,  $2\text{GY@Ag}_{\text{side}}$ ,  $2\text{GY@2Ag}_{\text{perpendicular}}$ ,  $2\text{GY@2Ag}_{\text{above}}$ , and  $2\text{GY@3Ag}_{\text{center}}$ . The effects of various graphyne surface based complexes on hyperpolarizabilities, frontier molecular orbitals (FMOs), density of states (DOS), absorption maximum ( $\lambda_{\text{max}}$ ), binding energy ( $E_{\text{b}}$ ), dipole moment ( $\mu$ ), electron density distribution map (EDDM), transition density matrix (TDM), electrostatic potential (ESP), vertical ionization energy ( $E_{\text{vi}}$ ) and electrical conductivity ( $\sigma$ ) have been investigated. Infrared (IR), non-covalent interaction (NCI) analysis accompanied by isosurface are performed to study the vibrational frequencies and type of interaction. Doping strategies in all complexes impressively reformed charge transfer characteristics such as narrowing band gap ( $E_{\text{g}}$ ) in the range of 2.58–4.73 eV and enhanced  $\lambda_{\text{max}}$  lying in the range of 368–536 nm as compared to pure GY with 5.78 eV  $E_{\text{g}}$  and 265 nm  $\lambda_{\text{max}}$  for ( $\text{GY@Ag}_{\text{center}}$ – $\text{GY@3Ag}_{\text{center}}$ ). In the case of ( $2\text{GY@Ag}_{\text{center}}$ – $2\text{GY@3Ag}_{\text{center}}$ ), when compared to 2GY with 5.58 eV  $E_{\text{g}}$  and 275 nm absorption, maximum doping techniques have more effectively modified  $\lambda_{\text{max}}$  in the region of 400–548 nm and  $E_{\text{g}}$ , which is in the order of 2.55–4.62 eV.  $\text{GY@3Ag}_{\text{center}}$  and  $2\text{GY@3Ag}_{\text{center}}$  reflected a noteworthy increment in linear polarizability  $\alpha_{\text{O}}$  (436.90 au) and (586 au) and the first hyperpolarizability  $\beta_{\text{O}}$  (5048.77 au) and (17 270 au) because of their lowest excitation energy ( $\Delta E$ ) when studied in comparison with GY ( $\alpha_{\text{O}} = 281.54$  and  $\beta_{\text{O}} = 0.21$  au) and 2GY surface ( $\alpha_{\text{O}} = 416$  and  $\beta_{\text{O}} = 0.06$  au). Focusing on harmony between the tiny Ag clusters and graphyne surface as well as their influences on NLO properties, graphyne doping using its two-unit cells (2GY) is found to be expedient for the development of future nanoscale devices.

Received 5th November 2021  
Accepted 20th January 2022

DOI: 10.1039/d1ra08117a

rsc.li/rsc-advances

## 1. Introduction

With the breakthroughs of the ruby laser in 1960 and the second harmonic generation (SHG) in 1961, Franklin and his

associates centralized their study on the non-linear optical (NLO) field, and this field turned into a progressive and distinctive discipline in interdisciplinary research.<sup>1</sup> NLO materials are turning out to be extremely prevalent on account of their probable uses in light emitters,<sup>2</sup> photonics,<sup>3</sup> optical switching<sup>4</sup> and holographic imaging<sup>5</sup> as well as electro-opto modulations.<sup>6</sup> For thirty years, NLO processes were mostly overlooked after being hypothesized in the 1930s. Recent hi-tech implementations encompass luminous materials gyroscopes,<sup>7</sup> frequency mixing, biosensor scanners,<sup>8</sup> SHG, and optical switching.<sup>9</sup> The computation of a substantial amount of data produced from diverse origins demands influential and proficient computers. Optical technology provides various methodologies of expanding information handling capabilities.<sup>10</sup> Increasing computing demands can be executed by NLO materials, for this reason, numerous modern organic and inorganic NLO active materials have been developed.<sup>11</sup>

<sup>a</sup>Department of Chemistry, University of Agriculture, Faisalabad-38000, Pakistan. E-mail: Javedkhattak79@gmail.com; Javed.iqbal@uaf.edu.pk

<sup>b</sup>Department of Chemistry, COMSATS University, Abbottabad Campus, Abbottabad-22060, Pakistan

<sup>c</sup>Punjab Bio-energy Institute, University of Agriculture, Faisalabad-38000, Pakistan

<sup>d</sup>Department of Physics, Sakarya University, Sakarya, Turkey

<sup>e</sup>Department of Physics, College of Science, Princess Nourah bint Abdulrahman University, P.O. Box 84428, Riyadh 11671, Saudi Arabia

<sup>f</sup>Research Center for Advanced Materials Science (RCAMS), King Khalid University, P. O. Box 9004, Abha 61413, Saudi Arabia

<sup>g</sup>Department of Physics, Faculty of Science, King Khalid University, P. O. Box 9004, Abha, Saudi Arabia

† Electronic supplementary information (ESI) available: Optimized cartesian coordinates of our studied compounds are also available. See DOI: 10.1039/d1ra08117a



Organic molecules based on NLO materials such as dibenzoboroles,<sup>12</sup> benzimidazoles, and chalcogens have been forefront in designing such materials due to their increased value of NLO coefficient, structural and electrical properties.<sup>13</sup> Because of desirable characteristics like greater thermal stability, facile synthesis, inexpensive, strength, and good transparency, inorganic molecules *i.e.*, phosphides and nitrides based NLO materials with considerable first or second hyperpolarizabilities had gained considerable research interest.<sup>14</sup> Significant variety of ordinary methodologies namely diradical character,<sup>15</sup> donor-acceptor  $\pi$  bridge system,<sup>16</sup> excess electron model,<sup>17</sup> and octupolar molecules<sup>18</sup> have been introduced to acquire ultrarapid high response NLO materials with exceptional hyperpolarizability.

GY,<sup>19</sup> as a novel non-natural carbon allotrope initially suggested by Baughman in 1987 (ref. 20) made up of sp-hybridized (ethynyl units) and sp<sup>2</sup>-hybridized (benzene rings) carbon<sup>21</sup> comparable to graphite/graphene (GR), has drawn the interest of researchers owing to its fascinating electrochemical, optoelectronic, and structural characteristics, as well as prospective microelectronic and power storage applications.<sup>22–25</sup> However, as far as we could possibly know the effect of doping of silver (Ag) cluster on the external layer of GY has yet to be accounted for. In view of this, the goal of this investigation is to determine the consequences of Ag cluster doping with GY on NLO and optoelectronic properties.

In this research project motivated by systematic exploration of graphyne, we performed simulations using one-unit celled graphyne as well as two-unit celled graphyne named as GY and 2GY respectively, five different Ag clusters doped with GY surface namely GY@Ag<sub>center</sub>, GY@Ag<sub>side</sub>, GY@2Ag<sub>perpendicular</sub>, GY@2Ag<sub>above</sub>, and GY@3Ag<sub>center</sub> are studied under model 1, each varying in orientation and number of dopant (Ag) on the surface (GY). Additionally, doping of Ag clusters on 2GY generated five different doped complexes namely 2GY@Ag<sub>center</sub>, 2GY@Ag<sub>side</sub>, 2GY@2Ag<sub>perpendicular</sub>, 2GY@2Ag<sub>above</sub>, and 2GY@3Ag<sub>center</sub> which are studied under model 2.

GY@Ag<sub>center</sub> and 2GY@Ag<sub>center</sub> possess one Ag atom doped on GY and 2GY at their center. GY@Ag<sub>side</sub> and 2GY@Ag<sub>side</sub> had one Ag atom doped at the sides of their surfaces. GY@2Ag<sub>perpendicular</sub>, as well as 2GY@2Ag<sub>perpendicular</sub> contain two Ag atoms doped in a perpendicular direction in the central cavity of GY and 2GY. GY@2Ag<sub>above</sub> and 2GY@2Ag<sub>above</sub> retain two Ag atoms just above the GY as well as 2GY surface. While GY@3Ag<sub>center</sub> and 2GY@3Ag<sub>center</sub> contain three Ag atoms in the central cavity of GY and 2GY. All of the doped complexes are found to be sufficiently stable. Fig. 1 shows a schematic diagram of model 1 and model 2.

## 2. Computational details

The Gaussian 09 simulation program<sup>26</sup> has been used to perform all computations for (GY@Ag<sub>center</sub>–2GY@3Ag<sub>center</sub>) and GY as well as 2GY. Structures of all molecules under category of model 1 are optimized using CAM-B3LYP<sup>27</sup> functional in association with the LANL2DZ basis set. While structures of complexes under the category of model 2 *i.e.* 2GY@Ag<sub>center</sub>, 2GY@Ag<sub>side</sub>, 2GY@2Ag<sub>perpendicular</sub>, 2GY@2Ag<sub>above</sub>, 2GY@3Ag<sub>center</sub> and 2GY are optimized using CAM-B3LYP/mixed basis. In mixed basis set of model 2 molecules, dopant (Ag) is optimized at LANL2DZ and 2GY surface *via* 6-31G basis set. To validate the type of computed geometries, frequency estimations were also conducted on the coordinates of optimized geometry. The molecular geometry, frontier molecular orbitals (FMOs), together with electrostatic potential (ESP) are extracted from optimized structures. UV-Vis spectral simulations of model 1 and model 2 are performed using time-dependent density functional theory (TD-DFT) along with their respective basis set with CAM-B3LYP functional. IEFPCM<sup>28</sup> is employed to specifically analyse the influence of H<sub>2</sub>O and CHCl<sub>3</sub> on absorption ( $\lambda_{\max}$ ) of complexes of model 1 and model 2 respectively. The  $\lambda_{\max}$  of researched molecules is processed in gas in addition to solvent phase. The Swizard program<sup>29</sup> has been used to compute spectral values and graphed with Origin 6.0 [22]. Interaction energies ( $E_{\text{int}}$ ) are approximated

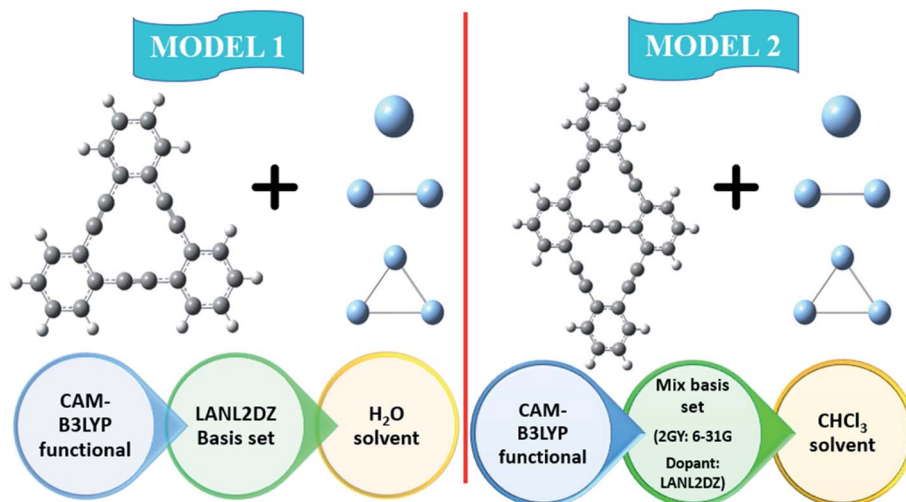


Fig. 1 Schematic diagram of model 1 as well as model 2.

using the following relation<sup>30</sup> to substantiate the thermodynamic stability of our doped surfaces (GY and 2GY).

$$E_{\text{int}} = E_{\text{d\_nGY}} - (E_{\text{nGY}} + E_{\text{n\_Ag}}) \quad (1)$$

Here,  $E_{\text{d\_nGY}}$ ,  $E_{\text{nGY}}$  and  $E_{\text{n\_Ag}}$  are energies of doped graphene, pure graphene, and  $n$  number of silver (Ag) and graphyne unit cells respectively. Vertical ionization energy ( $E_{\text{VI}}$ ) is also evaluated using eqn (2) (ref. 31) given below

$$E_{\text{VI}} = E_{\text{d\_nGY}}^+ - E_{\text{d\_nGY}} \quad (2)$$

Here,  $E_{\text{d\_nGY}}^+$  and  $E_{\text{d\_nGY}}$  represent cationic energy of Ag doped surfaces (GY and 2GY) and neutral energy of Ag doped surfaces (GY and 2GY). PyMOLyze 1.1 software<sup>32</sup> has been used to visualize DOS files while Multiwfn 3.7 tool<sup>33</sup> was used to determine electron densities. The same functional is also used electron density difference map (EDDM), dipole moment ( $\mu$ ), and infrared (IR) analysis. Hyperpolarizabilities are the most prevalent indicator of molecule's NLO response.

Through CAM-B3LYP/LANL2DZ basis set and CAM-B3LYP/mixed basis set, the  $\alpha_{\text{iso}}$  and  $\alpha_{\text{aniso}}$  (linear static polarizability), and  $\beta_{\text{static}}$  (first hyperpolarizability) are computationally estimated using expressions<sup>9,34</sup> given below

$$\alpha_0 = \frac{1}{3} (\alpha_{xx} + \alpha_{yy} + \alpha_{zz}) \quad (3)$$

$$\beta_0 = (\beta_x^2 + \beta_y^2 + \beta_z^2) \quad (4)$$

In equation,  $\beta_x = \beta_{xxx} + \beta_{xxy} + \beta_{xxz}$ ,  $\beta_y = \beta_{yyx} + \beta_{yyz} + \beta_{yxx}$ , and  $\beta_z = \beta_{zzx} + \beta_{zzx} + \beta_{zyy}$ .

## 3. Results and discussion

### 3.1 Geometry optimization

Optoelectronic characteristics are greatly influenced by molecular geometry. In model 1, CAM-B3LYP/LANL2DZ functional is used to optimize the pure GY as well as newly doped molecules (GY@Ag<sub>center</sub>–GY@3Ag<sub>center</sub>). Model 2 employs CAM-B3LYP/mixed basis set to optimize the pure 2GY as well as newly doped systems (2GY@Ag<sub>center</sub>–2GY@3Ag<sub>center</sub>). The front and side views of optimized frameworks of all molecules of model 1 and model 2 are shown in Fig. 2.

### 3.2 Photophysical properties

It's crucial to look at UV-visible spectra while researching electronic excitations and charge transfer. The absorption profile of model 1 having pure GY and doped complexes (GY@Ag<sub>center</sub>–GY@3Ag<sub>center</sub>) is computed with CAM-B3LYP/LANL2DZ functional in the gaseous phase and H<sub>2</sub>O solvent while that of model 2 via CAM-B3LYP/mixed basis set in gaseous phase and CHCl<sub>3</sub> solvent. The absorption profile of model 1 along with model 2 illustrates that all newly doped complexes are associated with higher wavelength than the GY surface in the gaseous phase as expressed in Fig. 3. Fig. 4 revealed that the employment of solvent as well as shifting toward higher unit cells of GY is due to stabilization of  $\pi$ -electrons.<sup>35</sup> GY@3Ag<sub>center</sub> has explored the

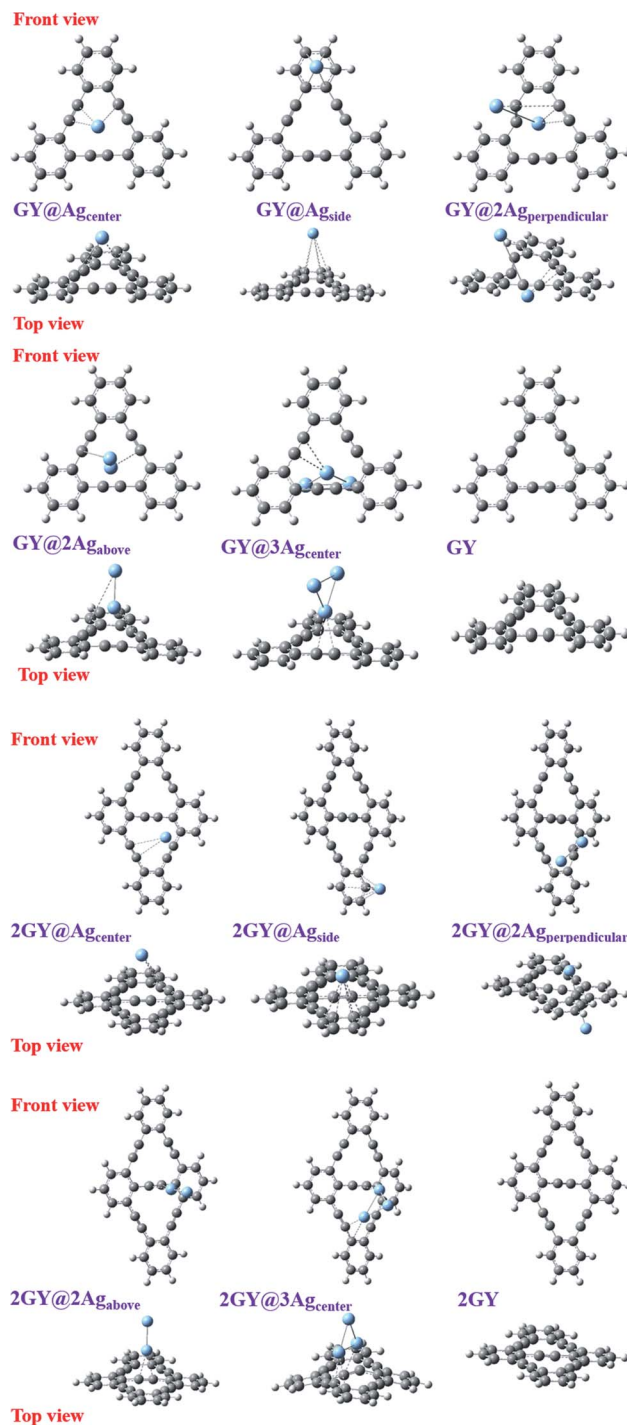


Fig. 2 Framework of all optimized structures from front and top views.

highest  $\lambda_{\text{max}}$  in the gaseous phase (522 nm) together with H<sub>2</sub>O phase (536 nm) amongst all molecules of model 1 due to the presence of three atoms of Ag on the GY surface. The  $\lambda_{\text{max}}$  of all complexes in solvent phase is increasing as GY < GY@Ag<sub>side</sub> < GY@Ag<sub>center</sub> < GY@2Ag<sub>above</sub> < GY@2Ag<sub>perpendicular</sub> < GY@3Ag<sub>center</sub>. Likewise, the highest  $\lambda_{\text{max}}$  in the gaseous phase (538 nm) as well as in the solvent phase (548 nm) among (2GY–2GY@3Ag<sub>center</sub>) complexes has been examined by 2GY@3Ag<sub>center</sub>.





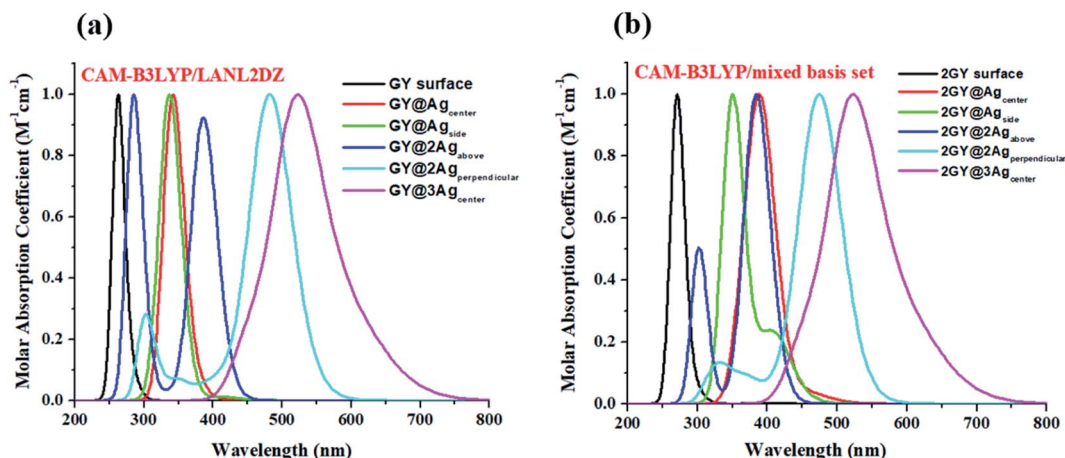


Fig. 3 UV-visible absorption graphs in gaseous phase of molecular complexes of (a) model 1 and (b) model 2.

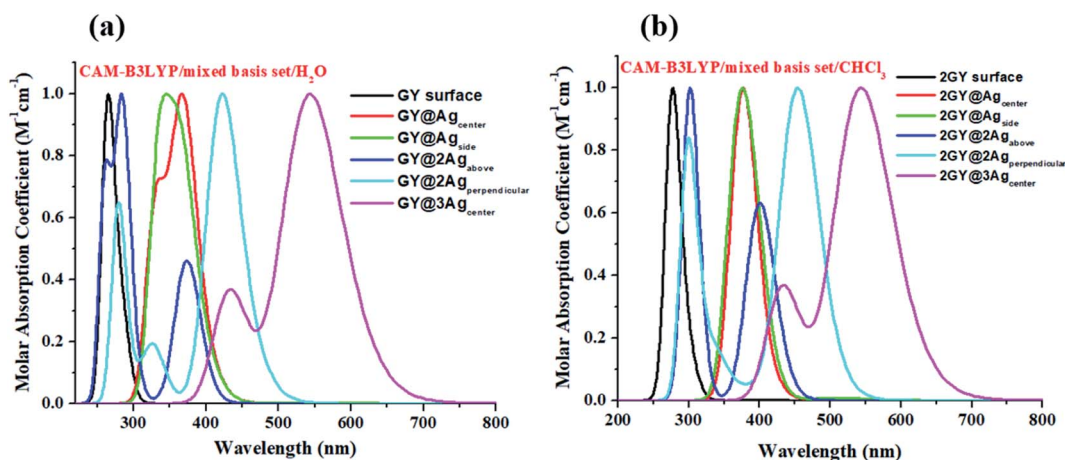


Fig. 4 UV-visible absorption graphs in solvent phase of molecular complexes of (a) model 1 and (b) model 2.

The band gap ( $E_g$ ) together with  $\lambda_{\max}$  are in intense correlation. Lower  $E_g$  makes the electronic excitation feasible. Narrow  $E_g$  is often interlinked to low kinetic stability since it is energetically preferable to remove electrons from low energy HOMO

or add electrons to high energy LUMO resulting in the formation of activated complexes. However, because of lower  $E_g$ , these doped systems can be regarded as n-type semiconductors.<sup>21</sup> These doped complexes have been regarded as novel members

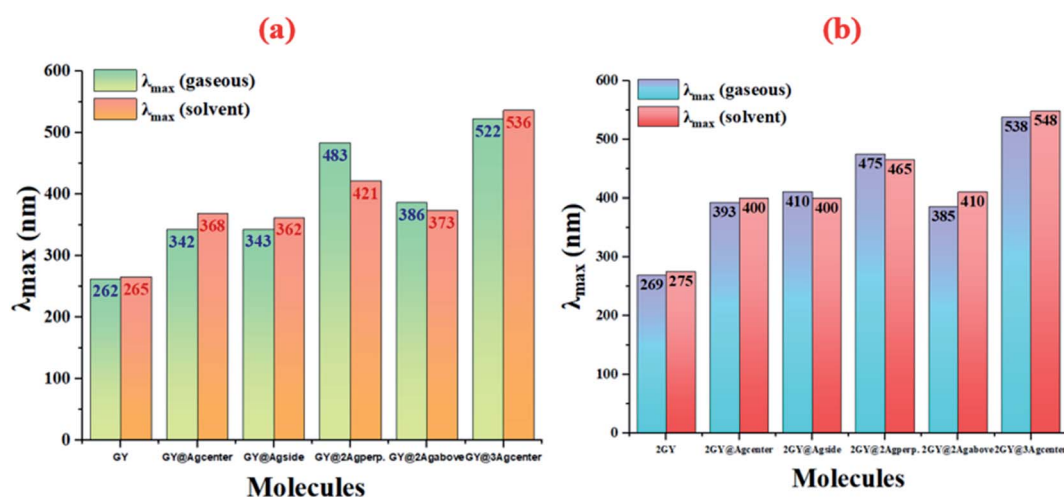
**Table 1** Computed  $\lambda_{\max}$ , excitation energy ( $E_{\text{opt}}$ ), highest oscillator strength  $f_{\text{OC}}$ , major molecular transitions of molecular systems of model 1 (GY–GY@3Ag<sub>center</sub>) and model 2 (2GY–2GY@3Ag<sub>center</sub>) in the gaseous phase

Molecules	$\lambda_{\max}$ (nm)	$E_{\text{opt}}$ (eV)	$f_{\text{OC}}$	Major molecular transitions (HOMO = H, LUMO = L)
GY	262	4.72	1.1619	H → L (69%)
GY@Ag <sub>center</sub>	342	3.62	0.0991	H → L (72%)
GY@Ag <sub>side</sub>	343	3.62	0.1043	H → L (90%)
GY@2Ag <sub>perpendicular</sub>	483	2.97	0.3980	H → L (66%)
GY@2Ag <sub>above</sub>	386	3.41	0.5394	H → L (70%)
GY@3Ag <sub>center</sub>	522	2.37	0.0923	H → L (100%)
2GY	269	4.60	2.2631	H → L (66%)
2GY@Ag <sub>center</sub>	393	3.15	0.0025	H → L (52%)
2GY@Ag <sub>side</sub>	410	2.97	0.0031	H → L (58%)
2GY@2Ag <sub>perpendicular</sub>	475	2.60	0.4104	H → L (67%)
2GY@2Ag <sub>above</sub>	385	3.22	0.5690	H → L (70%)
2GY@3Ag <sub>center</sub>	538	2.36	0.0923	H → L (76%)

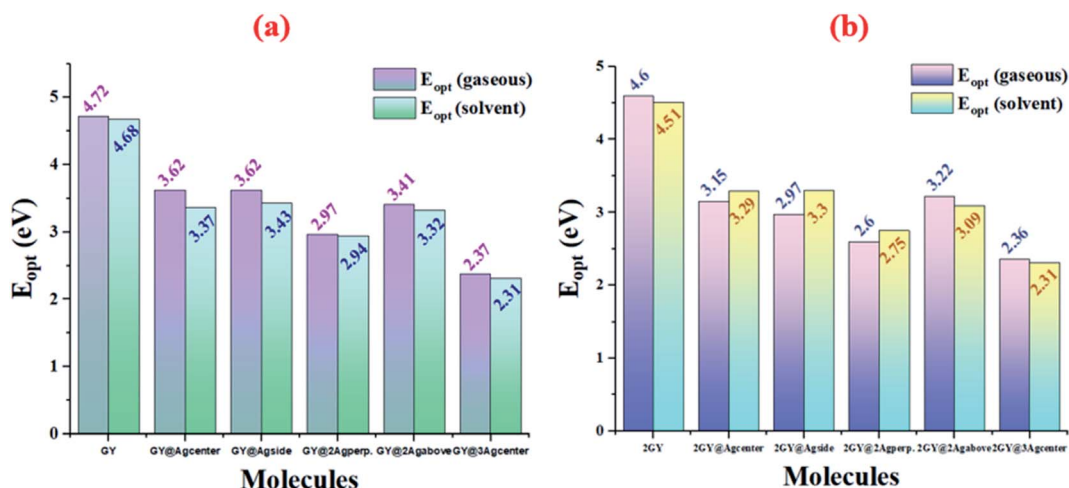


**Table 2** Computed  $\lambda_{\max}$ , excitation energy ( $E_{\text{opt}}$ ), highest oscillator strength  $f_{\text{OC}}$ , major molecular transitions of molecular systems of model 1 (GY–GY@3Agcenter) and model 2 (2GY–2GY@3Agcenter) in the solvent phase

Molecules	$\lambda_{\max}$ (nm)	$E_{\text{opt}}$ (eV)	$f_{\text{OC}}$	Major molecular transitions (HOMO = H, LUMO = L)
GY	265	4.68	1.1767	H → L (69%)
GY@Agcenter	368	3.37	0.1407	H → L (93%)
GY@Agside	362	3.43	0.1773	H → L (95%)
GY@2Ag <sub>perpendicular</sub>	421	2.94	0.4358	H → L (67%)
GY@2Ag <sub>above</sub>	373	3.32	0.6140	H → L (70%)
GY@3Agcenter	536	2.31	0.1283	H → L (100%)
2GY	275	4.51	2.5857	H → L (66%)
2GY@Agcenter	400	3.29	0.1376	H → L (82%)
2GY@Agside	400	3.30	0.0009	H → L (63%)
2GY@2Ag <sub>perpendicular</sub>	465	2.75	0.4577	H → L (76%)
2GY@2Ag <sub>above</sub>	410	3.09	0.6636	H → L (70%)
2GY@3Agcenter	548	2.31	0.1283	H → L (93%)



**Fig. 5** Graphical representation of comparison of absorption maximum ( $\lambda_{\max}$ ) in gaseous phase and solvent phase of (a) model 1 molecules (b) model 2 molecules.

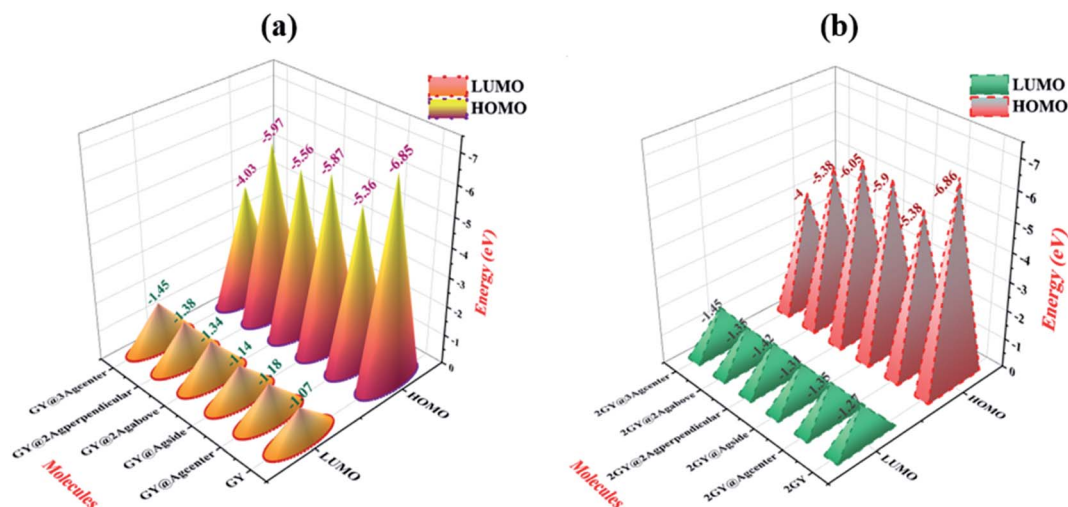


**Fig. 6** Graphical representation of comparison of excitation energy ( $E_{\text{opt}}$ ) in gaseous phase and solvent phase of (a) model 1 molecules (b) model 2 molecules.



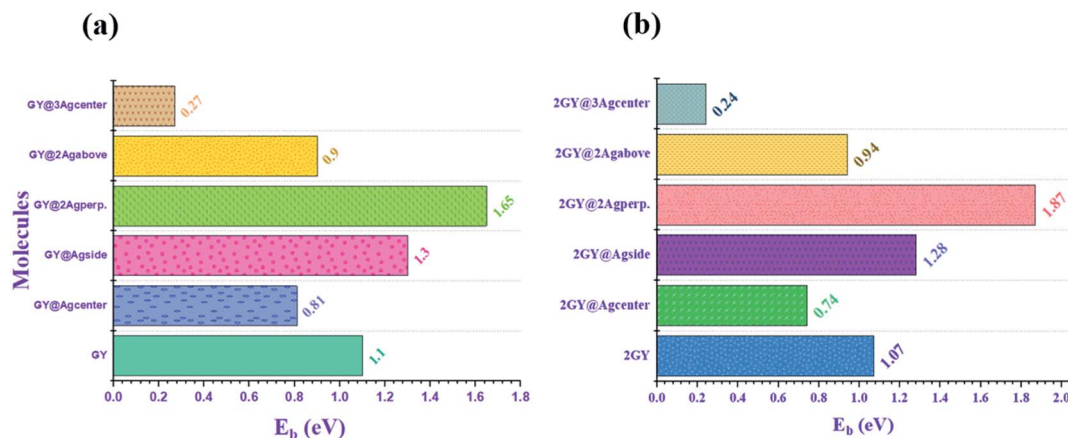
**Table 3** HOMO and LUMO energies,  $E_g$ , vertical ionization energies ( $E_{VI}$ ), interaction energies ( $E_{int}$ ) and binding energy ( $E_b$ ) of all investigated molecular complexes

Molecules	HOMO (eV)	LUMO (eV)	$E_g$ (eV)	$E_{VI}$ (eV)	$E_{int}$ (kcal mol <sup>-1</sup> )	$E_b$ (eV)
GY	-6.85	-1.07	5.78	6.85	—	1.1
GY@Ag <sub>center</sub>	-5.36	-1.18	4.18	5.36	-1.69	0.81
GY@Ag <sub>side</sub>	-5.87	-1.14	4.73	5.87	-0.97	1.3
GY@2Ag <sub>perpendicular</sub>	-5.97	-1.38	4.59	5.97	14.69	1.65
GY@2Ag <sub>above</sub>	-5.56	-1.34	4.22	5.56	-6.18	0.9
GY@3Ag <sub>center</sub>	-4.03	-1.45	2.58	4.03	-9.44	0.27
2GY	-6.86	-1.27	5.58	6.86	—	1.07
2GY@Ag <sub>center</sub>	-5.38	-1.35	4.03	5.38	-1.57	0.74
2GY@Ag <sub>side</sub>	-5.90	-1.31	4.58	5.90	-0.93	1.28
2GY@2Ag <sub>perpendicular</sub>	-6.05	-1.42	4.62	6.05	14.41	1.87
2GY@2Ag <sub>above</sub>	-5.38	-1.35	4.03	5.38	-5.95	0.94
2GY@3Ag <sub>center</sub>	-4.00	-1.45	2.55	4.00	-10.44	0.24

**Fig. 7** Graphical description of processed HOMO LUMO orbitals of (a) GY and (GY@Ag<sub>center</sub>–GY@3Ag<sub>center</sub>) and (b) 2GY and (2GY@Ag<sub>center</sub>–2GY@3Ag<sub>center</sub>).

of NLO materials. Values of  $\lambda_{max}$ , excitation energy ( $E_{opt}$ ) and oscillator strength ( $f_{OC}$ ) in both phases are summarized in Tables 1 as well as 2 respectively.

Results of tables confirmed that the employment of solvent has redshifted the  $\lambda_{max}$  of molecules of both models. Absorption ( $\lambda_{max}$ ) values of studied systems such as GY, GY@Ag<sub>center</sub>,

**Fig. 8** Graphical illustration of computed binding energy ( $E_b$ ) of (a) GY and (GY@Ag<sub>center</sub>–GY@3Ag<sub>center</sub>) and (b) 2GY and (2GY@Ag<sub>center</sub>–2GY@3Ag<sub>center</sub>).



GY@Ag<sub>side</sub>, GY@3Ag<sub>center</sub>, 2GY, GY@Ag<sub>center</sub>, GY@3Ag<sub>above</sub>, and GY@3Ag<sub>center</sub> are shifted to higher values in solvent. Like,  $\lambda_{\max}$  of pure surface GY and 2GY is 262 and 269 nm in gaseous phase; 265 and 275 nm in H<sub>2</sub>O owing to the stabilization of delocalized  $\pi$ -electrons.<sup>35</sup> Excitation energies ( $E_{\text{opt}}$ ) of all molecules are

lowered in solvents showing the ease of electron excitations in solvent phase as compared to the gaseous phase *i.e.*,  $E_{\text{opt}}$  of GY and 2GY is shifted from 4.72 and 4.60 eV to 4.68 and 4.51 eV.

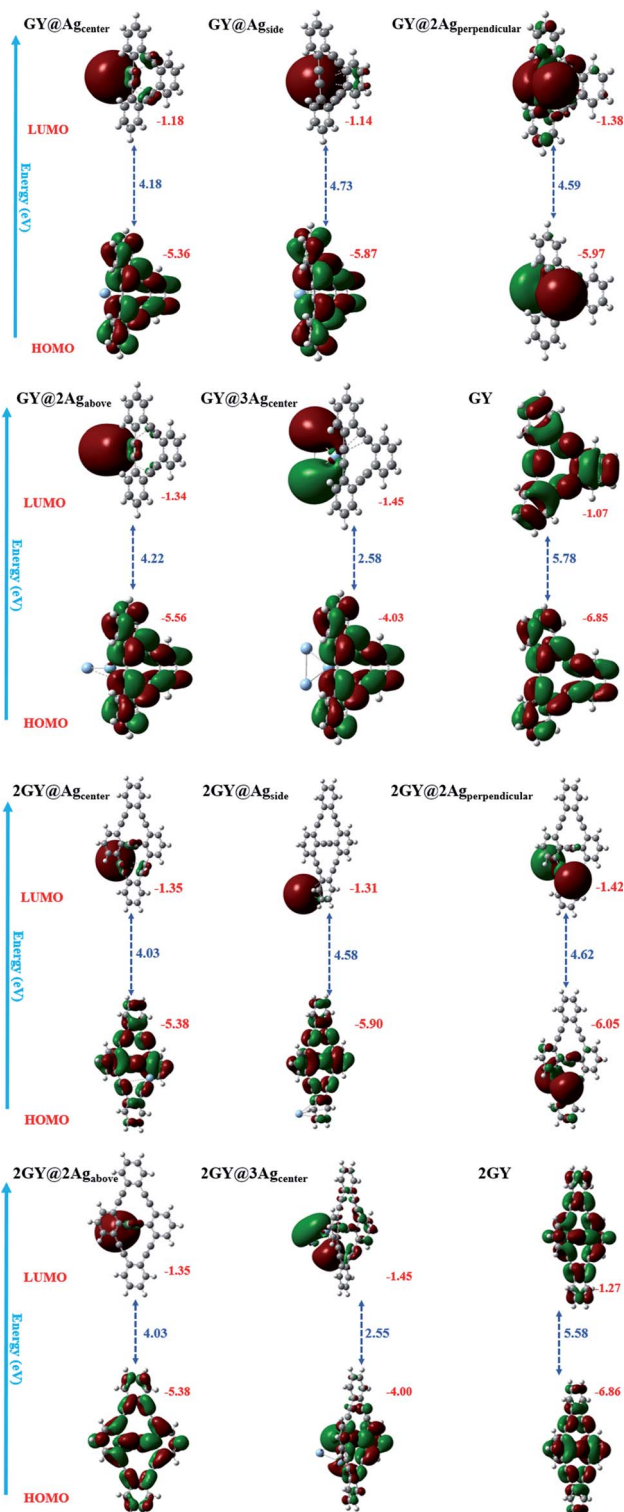


Fig. 9 FMO plots and band gaps ( $E_g$ ) of all studied complexes along with pure surfaces.

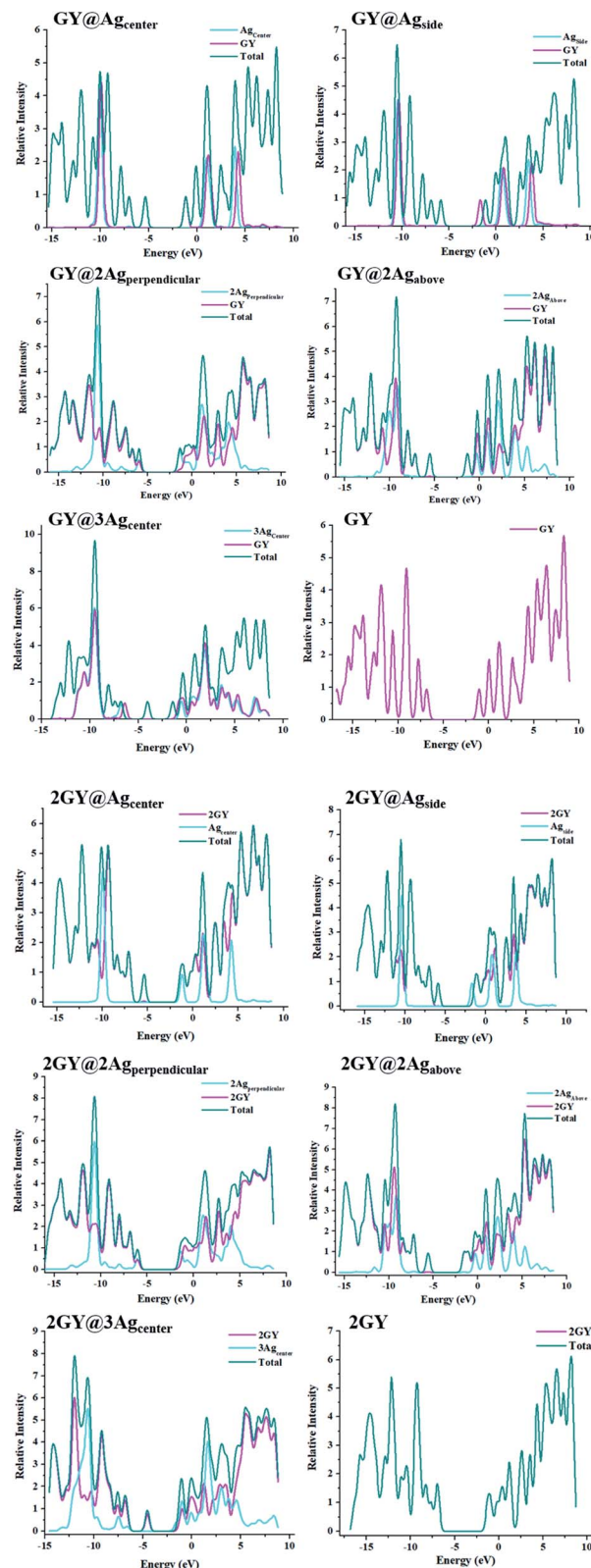


Fig. 10 DOS charts for molecules of model 1 and model 2.



**Table 4** Surface and dopant role in developing the HOMO and LUMO of surface and all doped complexes

Molecules	HOMO = H		Dopant
	LUMO = L	GY	
GY	H	100	—
	L	100	—
GY@Ag <sub>center</sub>	H	3.3	96.7
	L	100	0
GY@Ag <sub>side</sub>	H	0.6	99.4
	L	99.7	0.3
GY@2Ag <sub>perpendicular</sub>	H	47.2	52.8
	L	9.5	90.5
GY@2Ag <sub>above</sub>	H	2.4	97.6
	L	99.7	0.3
GY@3Ag <sub>center</sub>	H	0.6	99.4
	L	100	0
2GY	H	100	—
	L	100	—
2GY@Ag <sub>center</sub>	H	1.8	98.2
	L	97.0	3.0
2GY@Ag <sub>side</sub>	H	0.1	99.9
	L	99.3	0.7
2GY@2Ag <sub>perpendicular</sub>	H	1.0	99.0
	L	98.3	1.7
2GY@2Ag <sub>above</sub>	H	10.5	89.5
	L	47.6	52.4
2GY@3Ag <sub>center</sub>	H	18.8	81.2
	L	82.7	17.3

Shifting of molecular transitions to higher percentage also signifies ease of electronic excitation from HOMO to LUMO energy levels. Graphical comparative study of absorption maximum of all molecules of models 1 and 2 in gaseous and solvent phase is revealed in Fig. 5. Similarly, Fig. 6 illustrates graphical comparison of  $E_{\text{opt}}$  in gaseous and solvent phases.

It has been noted that photophysical properties revealed by doped systems of model 2 are associated with higher  $\lambda_{\text{max}}$  and lower  $E_{\text{opt}}$  due to extended conjugation in two-unit cells of GY.

### 3.3 Frontier molecular orbitals (FMOs)

Analyzing FMOs of molecules is an essential tool used to determine charge mobility.<sup>36</sup> It is also relevant in explaining the

**Table 5** Computed dipole moment of all doped complexes of model 1 and model 2 in gaseous phase ( $\mu_g$ ), excited phase ( $\mu_e$ ) and transition electric dipole moment ( $\Delta\mu$ )

Molecules	$\mu_g$ (D)	$\mu_e$ (D)	$\Delta\mu$ (au)
GY	0.001	0.001	3.157
GY@Ag <sub>center</sub>	1.455	1.218	0.940
GY@Ag <sub>side</sub>	0.975	0.570	0.004
GY@2Ag <sub>perpendicular</sub>	0.418	0.385	2.115
GY@2Ag <sub>above</sub>	3.479	2.556	2.588
GY@3Ag <sub>center</sub>	4.871	3.873	1.601
2GY	0.001	0.001	4.48
2GY@Ag <sub>center</sub>	1.349	1.191	0.97
2GY@Ag <sub>side</sub>	0.999	0.671	0.97
2GY@2Ag <sub>perpendicular</sub>	0.136	0.509	2.13
2GY@2Ag <sub>above</sub>	3.341	2.939	2.67
2GY@3Ag <sub>center</sub>	3.628	6.998	1.69

charge transfer and distribution patterns in doped systems. Molecular systems having the highest occupied (HOMO) and lowest unoccupied (LUMO) energies have a substantial impact on electronic properties and absorption attributes.<sup>37</sup> HOMO has condensed population electronic charge while LUMO has only high energy charges similar to the valence band and conduction band of band theory, respectively.

Band gap ( $E_g$ ) has been determined by following eqn (5).<sup>38</sup>

$$E_g = E_{\text{LUMO}} - E_{\text{HOMO}} \quad (5)$$

Here,  $E_{\text{LUMO}}$  and  $E_{\text{HOMO}}$  are LUMO and HOMO energies.

HOMO and LUMO energies together with their  $E_g$  are examined for both models 1 and 2 and their values are presented in Table 3. In pure GY and 2GY, HOMO lie at  $-6.85$  and  $-6.86$  eV respectively while their LUMOs lie at  $1.07$  and  $1.27$  eV with a  $E_g$  of  $5.78$  and  $5.58$  respectively. Practically charge mobility is governed by the  $E_g$ . Lower  $E_g$  allows the charge to be excited and transported more efficiently across the pi-conjugated system.  $E_g$  and electrical conductivity are intrinsically linked.  $E_g$  of all doped systems is narrow when compared to GY and lies at  $4.18$ ,  $4.73$ ,  $4.59$ ,  $4.22$ , and  $2.58$  eV for GY@Ag<sub>center</sub>, GY@Ag<sub>side</sub>, GY@2Ag<sub>perpendicular</sub>, GY@2Ag<sub>above</sub>, and GY@3Ag<sub>center</sub>.

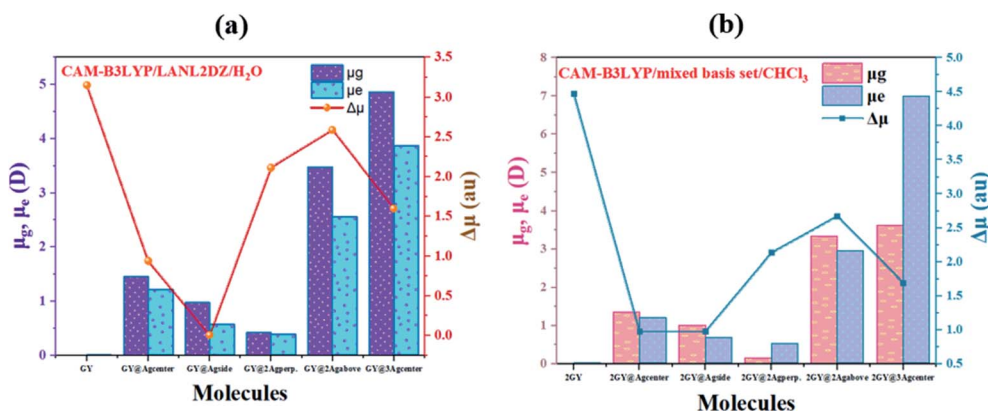


**Fig. 11** Graphical representation of dipole moments at ground ( $\mu_g$ ), excited ( $\mu_e$ ) and transition electric dipole moment ( $\Delta\mu$ ) of (a) GY and complexes GY@Ag<sub>center</sub>–GY@3Ag<sub>center</sub> and (b) 2GY and complexes 2GY@Ag<sub>center</sub>–2GY@3Ag<sub>center</sub>.





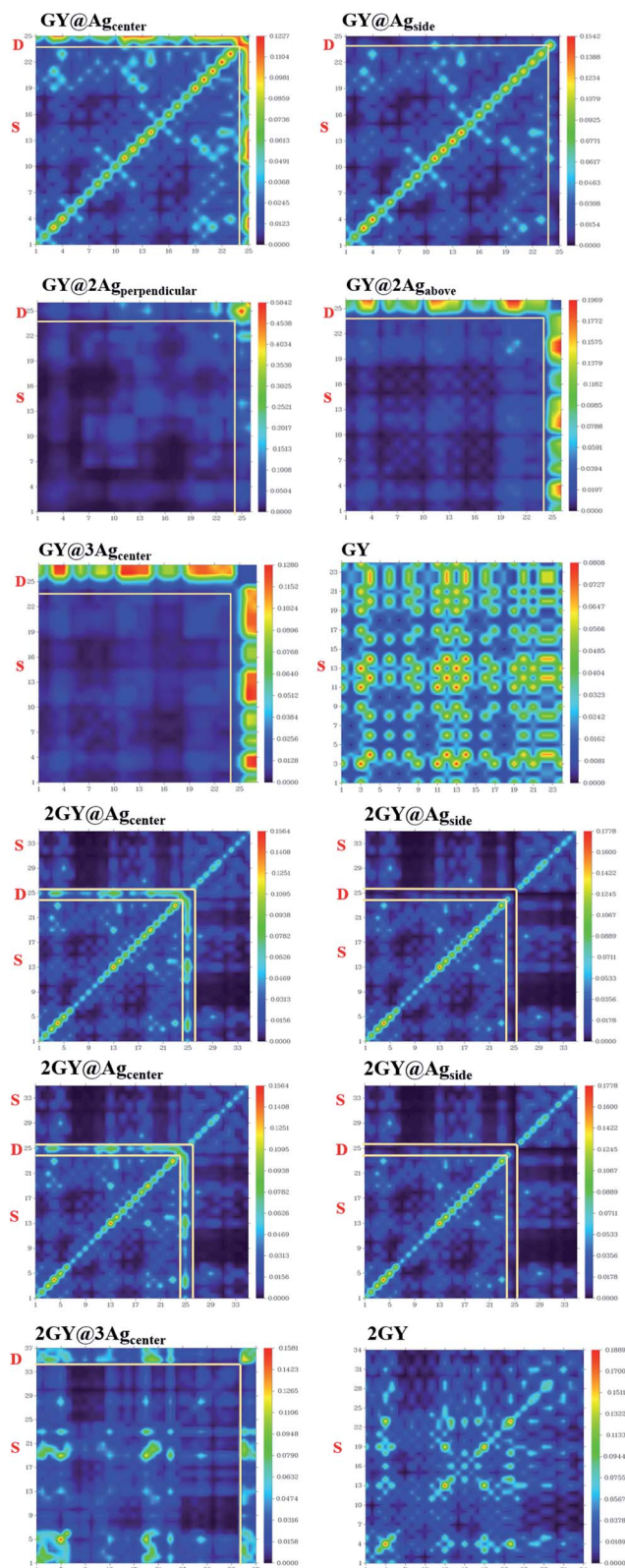


Fig. 12 TDM plots of pure surfaces and all molecular systems of model 1 and model 2. (a) GY and (GY@Ag<sub>center</sub>–GY@3Ag<sub>center</sub>) and (b) 2GY and (2GY@Ag<sub>center</sub>–2GY@3Ag<sub>center</sub>).

and GY@3Ag<sub>center</sub> respectively. Narrow  $E_g$  in GY@3Ag<sub>center</sub> validates enhanced conduction capacity. Due to low values  $E_g$ , all modeled doped systems (GY@Ag<sub>center</sub>–GY@3Ag<sub>center</sub>) are referred as polarizable, as well as efficient charge transfer complexes. Molecules of model 2 also indicated lower values of  $E_g$  as compared to their pure surface (2GY) and complexes of model 1 (GY–GY@3Ag<sub>center</sub>). Lowest  $E_g$  is shown by 2GY@3Ag<sub>center</sub> of 2.55 eV. Values of HOMOs and LUMOs are pictured in Fig. 7.

Internal energy ( $E_{\text{int}}$ ) refers to the stability of a molecule. Increase in  $E_{\text{int}}$  is associated with the increase in contact between dopant and surface, ultimately increasing the stability of the complex.<sup>39</sup> To study the thermodynamic stability of our doped complexes (GY@Ag<sub>center</sub>–GY@3Ag<sub>center</sub>) vertical ionization energy  $E_{\text{VI}}$  and  $E_{\text{int}}$  of complexes are determined computationally. From Table 3, it is inferred that values of  $E_{\text{int}}$  for GY@Ag<sub>center</sub>, GY@Ag<sub>side</sub>, GY@2Ag<sub>perpendicular</sub>, GY@2Ag<sub>above</sub>, and GY@3Ag<sub>center</sub> are  $-1.69$ ,  $-0.97$ ,  $14.69$ ,  $-6.18$ , and  $-9.44$  kcal mol<sup>-1</sup> respectively for model 1 complexes. Model 2 molecular systems, on the other hand, are more stable and possess strong interaction between 2Ag dopant in perpendicular direction with 2GY. Among all doped complexes, 2GY@2Ag<sub>perpendicular</sub> is the most stable as it possesses the highest  $E_{\text{int}}$ . Likewise, the highest  $E_{\text{VI}}$  is also revealed by 2GY@2Ag<sub>perpendicular</sub> verifying it is a stable complex among doped systems.

To acquire a better understanding of structural stability of complexes binding energy ( $E_b$ ) is computed theoretically.  $E_b$  of pure GY and 2GY surfaces as well doped systems (GY@Ag<sub>center</sub>–2GY@3Ag<sub>center</sub>) are calculated to explore the chemical stabilities using following eqn (6).<sup>40,41</sup>

$$E_b = E_g - E_{\text{opt}} \quad (6)$$

Here  $E_b$  is binding energy,  $E_g$  is band gap and  $E_{\text{opt}}$  is first excitation energy. Molecular systems possessing higher values of  $E_b$  are chemically stable and retain strong interaction between pure GY and dopants.<sup>21</sup> Among model 1 systems GY@Ag<sub>side</sub> and GY@2Ag<sub>perpendicular</sub> of newly doped systems explored higher values of  $E_b$  when compared to pure GY, confirming efficient

Table 6 Computed linear ( $\alpha_o$ ) and first hyperpolarizability ( $\beta_o$ ) of surface as well as doped complexes

Molecules	$\alpha_o$ (au)	$\beta_o$ (au)
GY	282	0.21
GY@Ag <sub>center</sub>	326	1797
GY@Ag <sub>side</sub>	333	1667
GY@2Ag <sub>perpendicular</sub>	368	2188
GY@2Ag <sub>above</sub>	371	2757
GY@3Ag <sub>center</sub>	437	5049
2GY	416	0.06
2GY@Ag <sub>center</sub>	460	1816
2GY@Ag <sub>side</sub>	469	1828
2GY@2Ag <sub>perpendicular</sub>	503	2449
2GY@2Ag <sub>above</sub>	506	2964
2GY@3Ag <sub>center</sub>	586	17 270



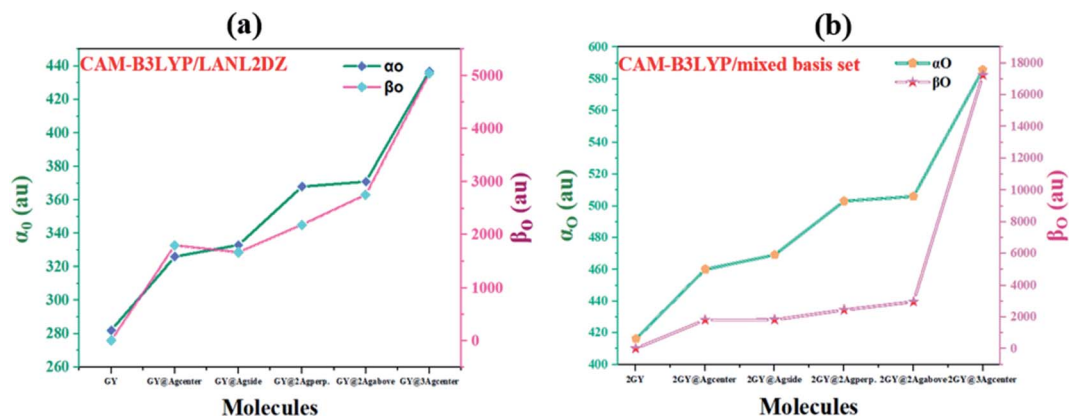


Fig. 13 Graphical representation of computed polarizabilities (a) GY and complexes GY@Ag<sub>center</sub>–GY@3Ag<sub>center</sub> and (b) 2GY and complexes 2GY@Ag<sub>center</sub>–2GY@3Ag<sub>center</sub>.

doping strategy on GY surface. Likewise, similar combinations of model 2 *i.e.*, 2GY@Ag<sub>side</sub> and 2GY@2Ag<sub>perpendicular</sub> showed higher  $E_b$ . While comparing the  $E_b$  of the two models, it was

noticed that all of the molecules in model 2 showed a change in  $E_b$  towards a higher value. Graphical representation of  $E_b$  of all complexes is shown in Fig. 8.

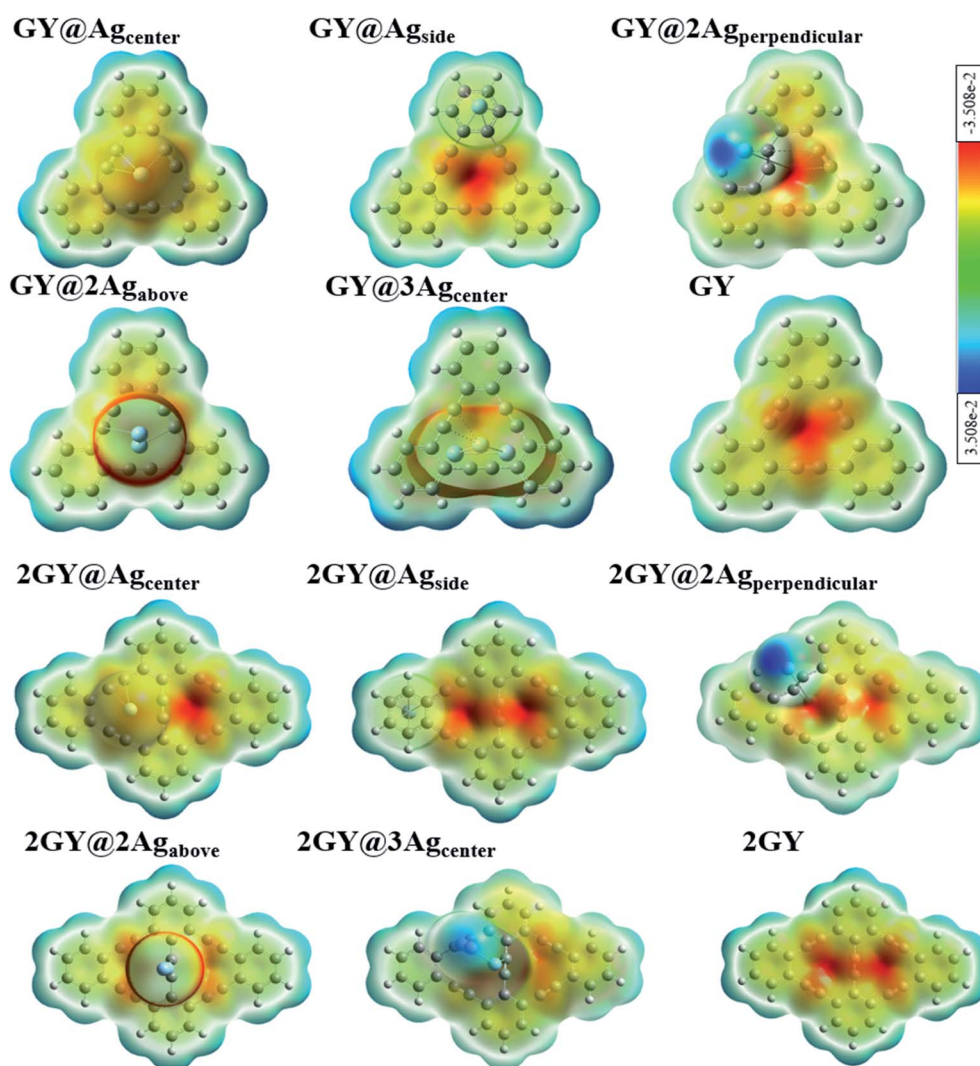


Fig. 14 ESP images of pure GY as well as GY@Ag<sub>center</sub>–GY@3Ag<sub>center</sub> and 2GY as well as 2GY@Ag<sub>center</sub>–2GY@3Ag<sub>center</sub>.



All analysed doped systems have their delocalization spread across the whole system.<sup>42</sup> In all complexes distribution pattern of energy orbitals is similar in a manner that HOMOs are concentrated over surfaces (GY) and (2GY) whereas LUMOs are condensed majorly on dopant and negligibly on surfaces.<sup>42</sup> FMO plots of pure GY and all studied molecules (GY@Ag<sub>center</sub>–2GY@3Ag<sub>center</sub>) along with their  $E_g$  are displayed in Fig. 9.

### 3.4 Density of states (DOS)

DOS is an analytical approach for analysing charge transport occupancy of states.<sup>43</sup> Mulliken charge distribution has supported FMO results. DOS research reveals how the fragmentation of the molecules raises the HOMO and LUMO molecular orbitals.<sup>44</sup> HOMO and LUMO energies can also be inferred *via* DOS approximations. DOS plots have been demonstrated to understand the role of the complexes and their fragments for

the investigation of chemical bandgap. The DOS graphs of all researched molecules are evinced in Fig. 10. Table 4 summarizes the participation of various sections in formulating of molecular orbitals. In GY and 2GY, both HOMO and LUMO are formed completely by the contribution of the surfaces. The influence of several sections in making of molecular orbitals in (GY@Ag<sub>center</sub>–GY@3Ag<sub>center</sub>) and (2GY@Ag<sub>center</sub>–2GY@3Ag<sub>center</sub>) is same. In these doped complexes, HOMO is acquired principally by the dopant and insignificantly by surfaces (GY and 2GY) while in the formation of LUMO GY and 2GY plays a substantial role.

### 3.5 Dipole moment ( $\mu$ )

The dipole moment ( $\mu$ ) plays a key role in molecular packing and crystallinity.<sup>45</sup> The more the crystalline material is, the less likely it is for charge transfer states to behave abnormally.<sup>46</sup> Dipole

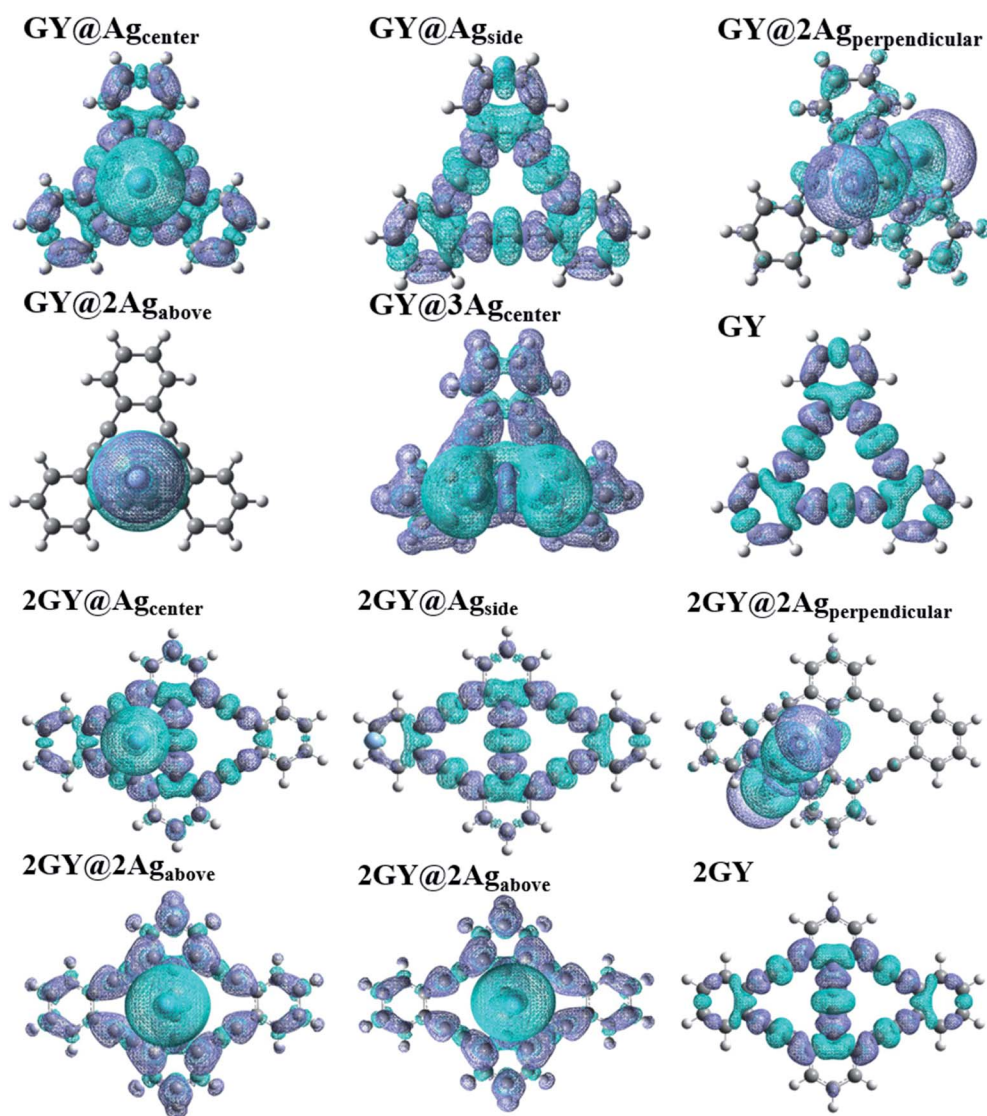


Fig. 15 EDDM images of pure GY as well as GY@Ag<sub>center</sub>–GY@3Ag<sub>center</sub> and 2GY as well as 2GY@Ag<sub>center</sub>–2GY@3Ag<sub>center</sub>.





moment in gaseous ( $\mu_g$ ), excited phase ( $\mu_e$ ) and transition electric dipole moment ( $\Delta\mu$ ) is estimated using CAM-B3LYP/LANL2DZ functional for model 1 molecules while model 2 molecular systems are discussed using CAM-B3LYP functional with mixed basis set. Computed values of dipole moments are reviewed in Table 5. Findings showed that all our doped molecules ( $\text{GY@Ag}_{\text{center}}\text{--GY@3Ag}_{\text{center}}$ ) and ( $2\text{GY@Ag}_{\text{center}}\text{--}2\text{GY@3Ag}_{\text{center}}$ ) acquired more  $\mu_g$  and  $\mu_e$  than their respective surfaces (GY and 2GY).

Pure GY and 2GY reveal lower  $\mu_g$  and  $\mu_e$  of 0.001 and 0.001 D respectively due to symmetry in its structure. Among all molecules of model 1,  $\text{GY@3Ag}_{\text{center}}$  revealed maximum value of  $\mu_g$  (4.871 D) and  $\mu_e$  (3.873 D) possessing three Ag atom clusters which facilitate self-assembly and aid in multilayer fabrication. Increasing order of  $\mu_e$  is  $\text{GY} < \text{GY@2Ag}_{\text{perpendicular}} < \text{GY@Ag}_{\text{side}} < \text{GY@Ag}_{\text{center}} < \text{GY@2Ag}_{\text{above}} < \text{GY@3Ag}_{\text{center}}$ . Same trend of increasing dipole moment is followed in the gaseous state. Hence, significant NLO properties can be achieved. Likewise, model 2 molecules also illustrated a significant shift towards high value in comparison with 2GY and model 1 system. The impressive change in  $\mu$  infers that complexes have arrayed themselves so as to limit recombination of charges. Dipole moments are graphically illustrated in Fig. 11.

### 3.6 Transition density matrix (TDM)

TDM refers to the matrix that dispenses information about charge transition locations and quantum geometry of doped molecules in excited state.<sup>47,48</sup> In TDM plots, the number of atoms is given on the x-axis and y-axis (left side) while on the right side of the y-axis coefficient of transition or electron density is displayed. Using the specified hybrid DFT functional, TDM analysis of pure GY and 2GY and currently doped molecules ( $\text{GY@Ag}_{\text{center}}\text{--GY@3Ag}_{\text{center}}$ ) and ( $2\text{GY@Ag}_{\text{center}}\text{--}2\text{GY@3Ag}_{\text{center}}$ ) has been accomplished. Because of insignificant contributions in transitions, hydrogens atoms have been overlooked. Fig. 12 shows a visual representation of all molecules. GY and 2GY are divided into one component while all other systems are sequestered into two fractions: surface and dopant.

In pure GY and 2GY, charge distribution and coherency can be accomplished by valuable diagonal as well as off-diagonal charge transfer. In all designed doped materials, electronic distribution is concentrated on dopant portions. The bright spots on TDM are pointing to the atom number where the transition population was detected. The doped materials had exhibited enhanced charge transfer from surface to dopant. So, ( $\text{GY@Ag}_{\text{center}}\text{--GY@3Ag}_{\text{center}}$ ) and ( $2\text{GY@Ag}_{\text{center}}\text{--}2\text{GY@3Ag}_{\text{center}}$ ) exhibit marvellous charge separation capability when studied in contrast to pure GY and 2GY, as a result, they can be used as unintentional aspirants for future NLO materials with improved characteristics.

### 3.7 NLO properties

The most persuasive parameter to quantify the NLO properties of pure GY and doped materials is linear polarizability ( $\alpha_0$ ) first hyperpolarizability ( $\beta_0$ ).<sup>49</sup> Both  $\alpha_0$  and  $\beta_0$  of all molecules of model 1 and 2 are evaluated computationally at their respective

functionals and basis set, and outcomes are disclosed in Table 6. Values of  $\alpha_0$  and  $\beta_0$  of all complexes ( $\text{GY@Ag}_{\text{center}}\text{--GY@3Ag}_{\text{center}}$ ) are contrasted with pure GY.  $\alpha_0$  of pure GY

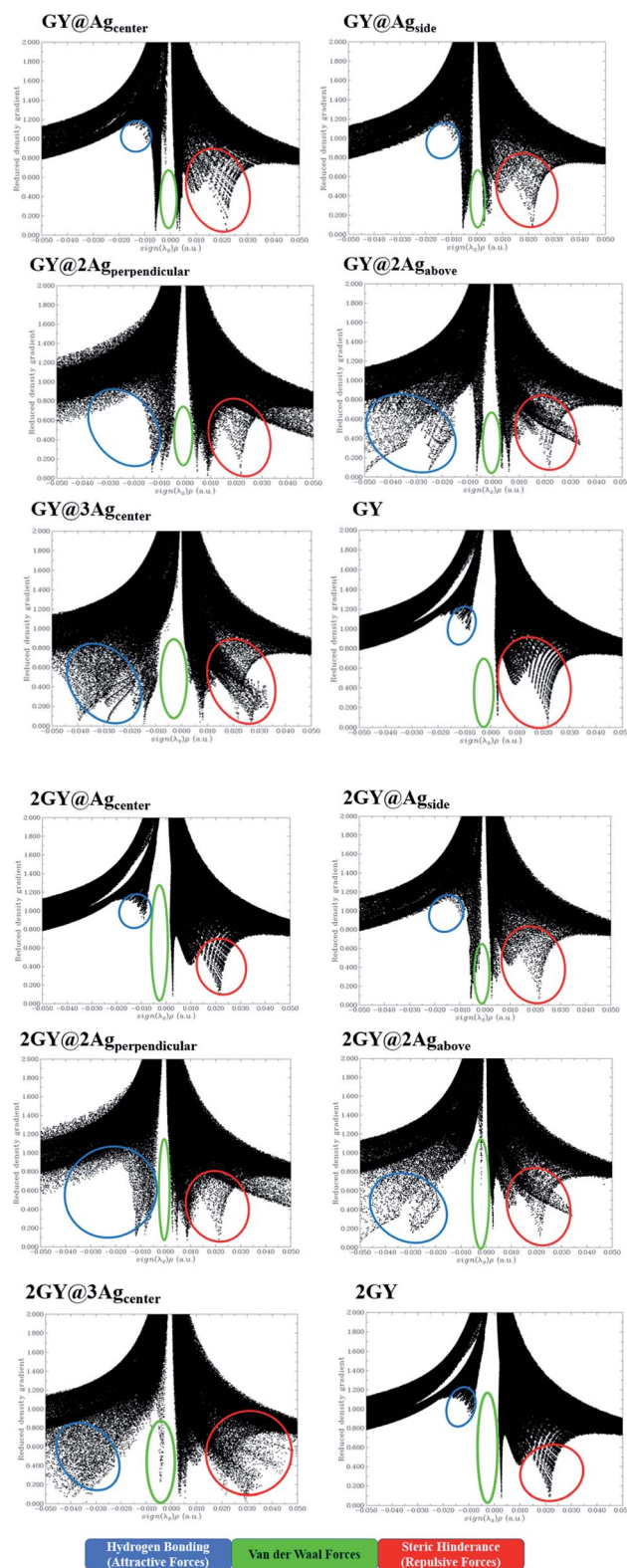


Fig. 16 NCI images for molecular complexes of model 1 as well as model 2.



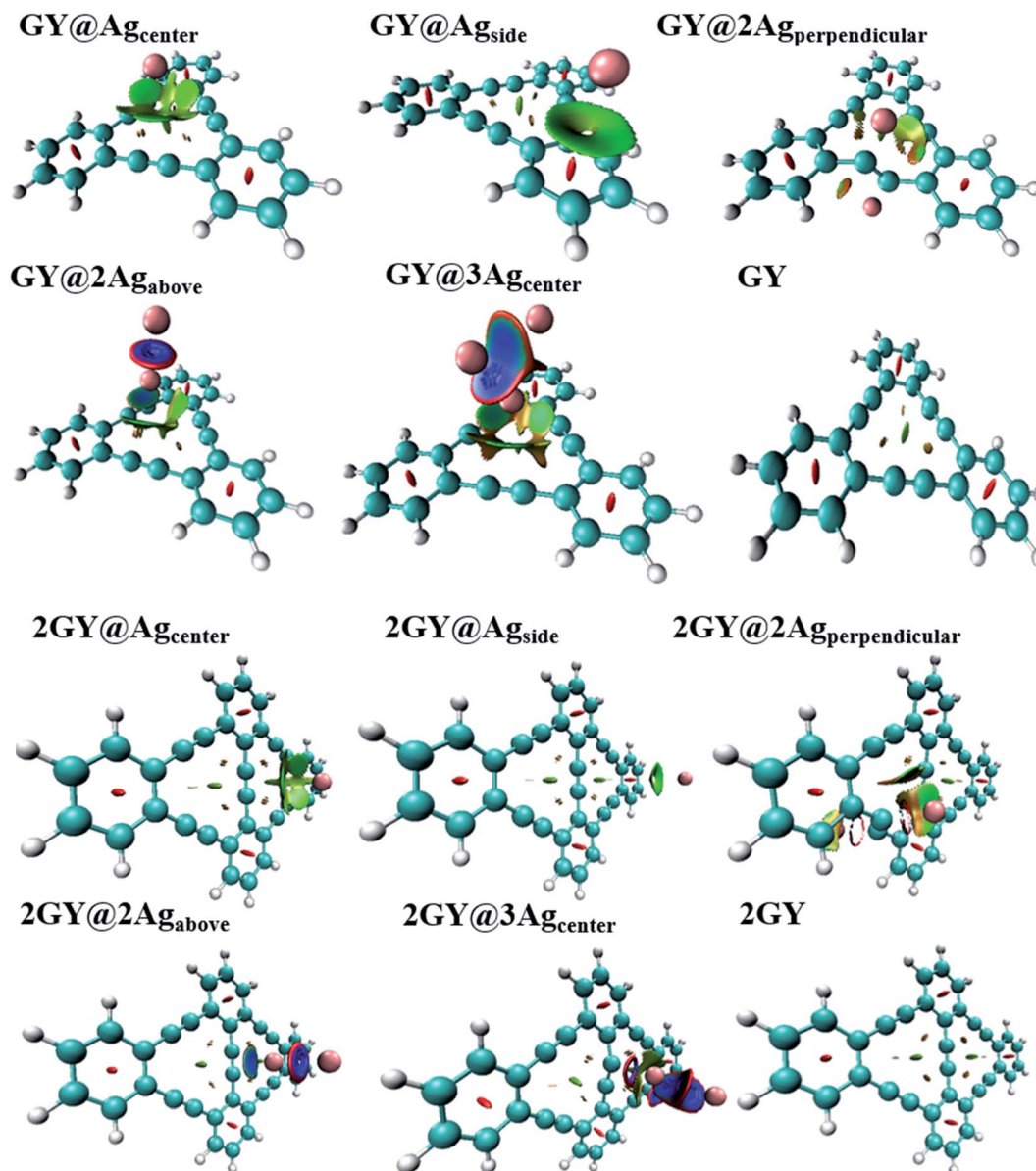


Fig. 17 Pictorial representation of 3D isosurface of all molecular complexes of model 1 as well as model 2.

surface lies at 282 au while doping of Ag clusters had prominently increased  $\alpha_O$  in all doped complexes.  $\alpha_O$  of  $\text{GY@Ag}_{\text{center}}$ ,  $\text{GY@Ag}_{\text{side}}$ ,  $\text{GY@2Ag}_{\text{perpendicular}}$ ,  $\text{GY@2Ag}_{\text{above}}$ , and  $\text{GY@3Ag}_{\text{center}}$  are 326, 333, 368, 371, and 437 au respectively. 55% increase in linear polarizability  $\alpha_O$  of  $\text{GY@3Ag}_{\text{center}}$  (437 au) is observed considering  $\text{GY}$  surface as a reference.

According to the literature, the NLO performance of a doped complex can be substantially intensified by the incorporation of surplus electrons. High energy HOMO levels are occupied by surplus electrons, leading to a decrease in  $E_g$  and elevation in  $\beta_O$ .<sup>10</sup>  $\beta_O$  of pure  $\text{GY}$  calculated computationally is 0.21 au. Pronounced shift in  $\beta_O$  of all doped complexes ( $\text{GY@Ag}_{\text{center}}$ – $\text{GY@3Ag}_{\text{center}}$ ) is observed. The  $\beta_O$  of all investigated complexes is decreasing as  $\text{GY@3Ag}_{\text{center}}$  (5049 au) >  $\text{GY@2Ag}_{\text{above}}$  (2757 au) >  $\text{GY@2Ag}_{\text{perpendicular}}$  (2188 au) >  $\text{GY@Ag}_{\text{center}}$  (1797 au) >  $\text{GY@Ag}_{\text{side}}$  (1667 au) >  $\text{GY}$  (0.21 au). Molecular systems of model

2 ( $2\text{GY@Ag}_{\text{center}}$ – $2\text{GY@3Ag}_{\text{center}}$ ) indicated sharp increase in  $\alpha_O$  and  $\beta_O$  of complexes.  $2\text{GY@3Ag}_{\text{center}}$  acquired  $\beta_O$  of 17 270 au. The graphical representation of  $\alpha_O$  and  $\beta_O$  is pictured in Fig. 13, representing  $\beta_O$  has increased several folds when studied in comparison with  $\text{GY}$ . Keeping in view the analysis of NLO properties, it is inferred that all our designed doped complexes specially complexes having two-unit cells of  $\text{GY}$  i.e., ( $2\text{GY@Ag}_{\text{center}}$ – $2\text{GY@3Ag}_{\text{center}}$ ), will exhibit magnificent NLO responses.

### 3.8 Electron density and electrostatic potential (ESP) analysis

Electron density (ED) analysis grasps information regarding the reactivity of atoms and the presence of reactive sites for nucleophilic and electrophilic attack based on the distribution of the



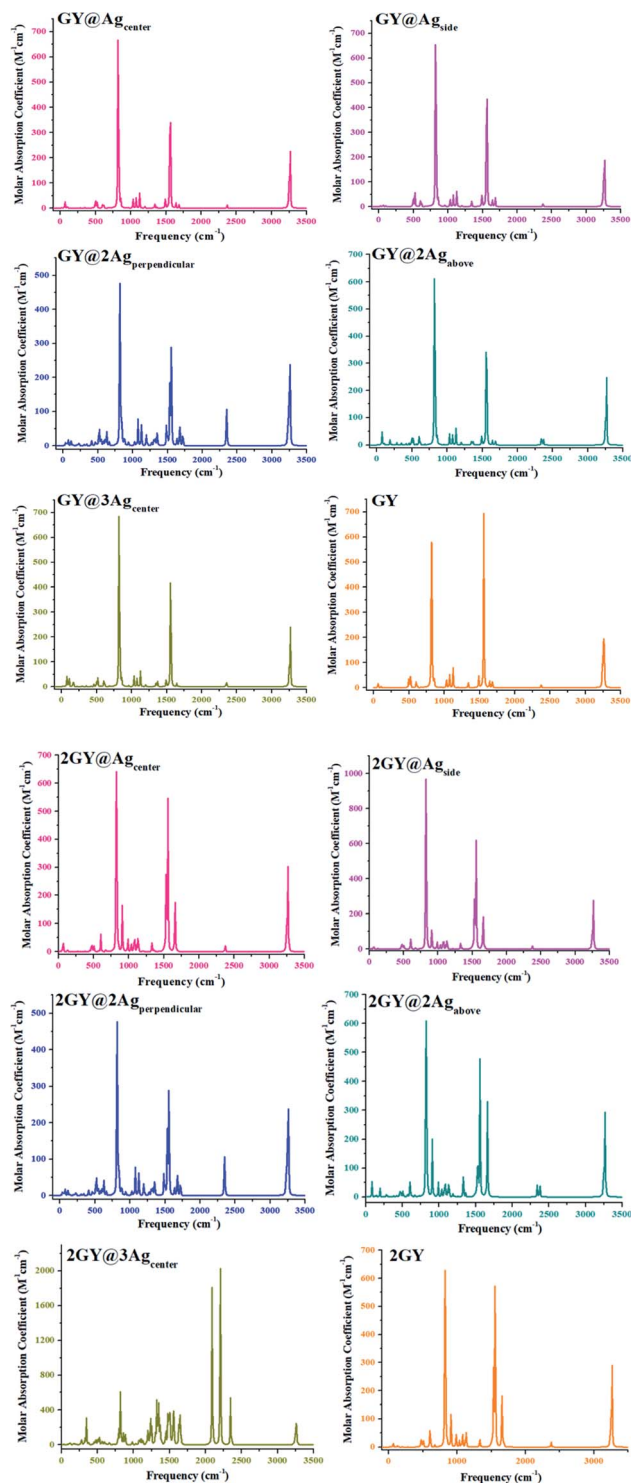


Fig. 18 IR plots of pure surfaces and all molecular systems of model 1 and model 2.

Milliken charge on the whole molecule.<sup>50</sup> ESP is also crucial in predicting the correlation among molecular structure, molecular interaction, as well as photophysical properties of molecules.<sup>51</sup> The electrophilic and nucleophilic regions of researched molecules are determined using ESP simulations conducted at optimal DFT functional. In ESP diagrams, red hue

reflects the electrophilic, electron rich and negative ESP zone whereas the green hue signifies neutral zone, and the blue hue is concentrated on the nucleophilic, electrons deficient and positive ESP zone.<sup>36</sup>

ESP analysis of all doped complexes along with GY and 2GY is done theoretically. Fig. 14 shows ESP diagrams of the pure surfaces along with freshly doped complexes. ESP diagrams of complexes of model 1 and model 2 demonstrate that the red color (negative potential) is concentrated on the acetylene region of the graphyne surface making it more electrophilic. The region where Ag dopant exists and backbone chain of surface in each molecular framework ( $\text{GY@Ag}_{\text{center}}$ – $\text{GY@3Ag}_{\text{center}}$ ) and ( $2\text{GY@Ag}_{\text{center}}$ – $2\text{GY@3Ag}_{\text{center}}$ ), possess blue color (positive potential) and behave as a nucleophile.

### 3.9 Electron density distribution matrix (EDDM)

To comprehend the charge transfer capacity, EDDM evaluations were also executed in which molecular orbitals of excited state are subtracted from ground state.<sup>52</sup> EDDM of all doped complexes ( $\text{GY@Ag}_{\text{center}}$ – $\text{GY@3Ag}_{\text{center}}$ ) along with GY is evaluated computationally at CAM-B3LYP/LANL2DZ functional while analysis of ( $2\text{GY@Ag}_{\text{center}}$ – $2\text{GY@3Ag}_{\text{center}}$ ) is done at CAMB3LYP/mixed basis set. EDDM graphs show the reorganization of electrons in pure surfaces and doped complexes. Fig. 15 shows the net charge density of subtracted complexes. Sea-green color in EDDM diagrams reveals a positive value of charge density while purple color illustrates the negative value and reduced electron density upon excitation. Charge distribution pattern in GY, 2GY,  $\text{GY@Ag}_{\text{center}}$ ,  $2\text{GY@Ag}_{\text{center}}$ ,  $\text{GY@Ag}_{\text{side}}$ ,  $2\text{GY@Ag}_{\text{side}}$ ,  $2\text{GY@2Ag}_{\text{above}}$ , and  $\text{GY@3Ag}_{\text{center}}$ ,  $2\text{GY@3Ag}_{\text{center}}$ , is analogous, in such a way that charge density is distributed evenly over the entire system. But in  $\text{GY@2Ag}_{\text{perpendicular}}$ ,  $2\text{GY@2Ag}_{\text{perpendicular}}$ , and  $\text{GY@2Ag}_{\text{above}}$  charge distribution is mainly concentrated on dopant units.

### 3.10 Non-covalent interaction (NCI) analysis

The NCI assessment gives valuable information regarding a molecule's non-covalent interactions.<sup>53</sup> NCI plot can distinguish between the molecular areas with weak interactions and those with strong directional attractions associated with localised atom–atom linkages.<sup>54</sup> Fig. 16 depicts the scatter graphs drawn between the reduced density gradient and the electron density ( $r$ ), oriented by the sign of  $\lambda_2$ .<sup>55</sup> NCI analysis appears to be a superior alternative for using data about hydrogen bonding, van der Waals forces, and steric hindrance inside a system to improve information on the molecular stability in small or large molecules.<sup>55</sup> The scatter graphs are created with Multiwfn software. The  $(\lambda_2) \rho$  values can be used to predict the nature of interaction: if  $(\lambda_2) \rho > 0$  then the interaction is repulsive, and if  $(\lambda_2) \rho < 0$  then the interaction is attractive that is also highlighted by color-filled 3D isosurface of complexes and graphyne, shown in Fig. 16. The NCI graphs of all doped systems along with surfaces (GY and 2GY) show that strong attractive forces exist between the complex molecules that is advantageous for propitious NLO materials. The H-bond





Table 7 Computed IR frequencies of pure surface as well as all doped complexes

Molecules	Frequency (cm <sup>-1</sup> )	Vibrations	Molecules	Frequency (cm <sup>-1</sup> )	Vibrations
<b>GY</b>	64	Wagging	<b>2GY</b>	75	Wagging
	824	Twisting		822	Twisting
	1561	Scissoring		1557	Scissoring
	3266	Symmetrical stretching		3267	Symmetrical stretching
<b>GY@Ag<sub>center</sub></b>	66	Wagging	<b>2GY@Ag<sub>center</sub></b>	64	Wagging
	824	Twisting		825	Twisting
	1560	Scissoring		1557	Scissoring
	3266	Symmetrical stretching		3267	Symmetrical stretching
<b>GY@Ag<sub>side</sub></b>	64	Wagging	<b>2GY@Ag<sub>side</sub></b>	76	Wagging
	823	Twisting		828	Twisting
	1561	Scissoring		1557	Scissoring
	3267	Symmetrical stretching		3255	Symmetrical stretching
<b>GY@2Ag<sub>perpendicular</sub></b>	74	Wagging	<b>2GY@2Ag<sub>perpendicular</sub></b>	74	Wagging
	822	Twisting		822	Twisting
	1535	Scissoring		1535	Scissoring
	2348	Asymmetrical stretching		2348	Asymmetrical stretching
<b>GY@2Ag<sub>above</sub></b>	3264	Symmetrical stretching	<b>2GY@2Ag<sub>above</sub></b>	3264	Symmetrical stretching
	77	Wagging		96	Wagging
	823	Twisting		825	Twisting
	1561	Scissoring		1553	Scissoring
<b>GY@3Ag<sub>center</sub></b>	3268	Symmetrical stretching	<b>2GY@3Ag<sub>center</sub></b>	3266	Symmetrical stretching
	80	Scissoring		84	Scissoring
	823	Twisting		823	Twisting
	1558	Scissoring		2204	Scissoring
	3268	Symmetrical stretching		3264	Symmetrical stretching

(attractive) is shown by the blue tone, the van der Waals interactions are indicated by the green hue, and the steric effect is indicated by the red region (repulsive) (Fig. 17).

### 3.11 Infrared (IR) analysis

Infrared (IR) spectrum characteristics of pure graphyne and doped complexes are researched to analyze how they change with doping. Fig. 18 depicts the IR spectrum. In all IR spectra, frequencies around 64 to 77 cm<sup>-1</sup> are due to wagging vibrations except for **GY@3Ag<sub>center</sub>** and **2GY@3Ag<sub>center</sub>** where 80 cm<sup>-1</sup> frequency is for scissoring vibrations. Vibrational frequencies at around 800 cm<sup>-1</sup>, 1550 cm<sup>-1</sup>, and 3200 cm<sup>-1</sup> in all systems are related to twisting, scissoring, and symmetrical stretching vibrations. Detailed study of vibrational frequencies of all studied molecules is illustrated in Table 7.

### 3.12 Electrical conductivity ( $\sigma$ )

Most crucial aspect in determining the electrical conductivity ( $\sigma$ ) of doped complexes for NLO properties is  $E_g$ . After adsorbing the silver (Ag) clusters on the surface (**GY** and **2GY**), these unique complexes (**GY@Ag<sub>center</sub>**–**GY@3Ag<sub>center</sub>**) and (**2GY@Ag<sub>center</sub>**–**2GY@3Ag<sub>center</sub>**) become more semiconductor-like owing to their narrow  $E_g$ . Therefore, it is envisaged that the  $\sigma$  is increased as compared to pure surface and can be determined using eqn (6).<sup>56</sup>

$$\sigma \propto \exp\left(\frac{-E_g}{2kT}\right) \quad (7)$$

Here,  $\sigma$  is electrical conductivity,  $E_g$  is the band gap,  $k$  is Boltzmann constant and  $T$  is the temperature in kelvin. From

the equation, it is inferred that the doped complexes possessing lower  $E_g$  will have higher  $\sigma$  because it is exponentially correlated to  $E_g$ .<sup>57</sup> In our investigation of model 1 systems,  $E_g$  of all newly designed doped complexes has smaller values (in the range of 2.58 to 4.73 eV) in comparison with pure **GY** (5.78 eV) as indicated in Table 3 leading to the significant increase in electrical conductivities of doped complexes (**GY@Ag<sub>center</sub>**–**GY@3Ag<sub>center</sub>**). Likewise, all molecular systems (**2GY@Ag<sub>center</sub>**–**2GY@3Ag<sub>center</sub>**) are accompanied by relatively lower  $E_g$  and higher electrical conductivity ( $\sigma$ ). Electrical conductivity of complexes lies in the order of **2GY@3Ag<sub>center</sub>** > **2GY@Ag<sub>center</sub>** = **2GY@2Ag<sub>above</sub>** > **2GY@Ag<sub>side</sub>** > **2GY@2Ag<sub>perpendicular</sub>** > **2GY**. An increase in  $\sigma$  has resulted from strong dopant–surface interaction and efficient  $n \rightarrow \sigma^*$  charge transfer. Thus, our designed Ag cluster doped complexes on the **2GY** surface may behave as unique sensing materials.

## 4. Conclusion

The current study relies on the comprehensive analysis of Ag cluster doped with graphyne surface in two distinct ways. In model 1, one-unit cell graphyne (**GY**) doped with variable Ag clusters produced complexes namely **GY@Ag<sub>center</sub>**, **GY@Ag<sub>side</sub>**, **GY@2Ag<sub>perpendicular</sub>**, **GY@2Ag<sub>above</sub>**, **GY@3Ag<sub>center</sub>** and employ CAM-B3LYP/LANL2DZ functional to explore the NLO properties. While in model 2, two-unit cell graphyne (**2GY**) doped with Ag are designed namely **2GY@Ag<sub>center</sub>**, **2GY@Ag<sub>side</sub>**, **2GY@2Ag<sub>perpendicular</sub>**, **2GY@2Ag<sub>above</sub>**, **2GY@3Ag<sub>center</sub>** and their NLO properties are studied at CAM-B3LYP/mixed basis set. To study charge distribution FMOs, DOS, EDDM, TDM, and ESP



analysis were directed. Using  $E_{\text{VI}}$  and  $E_{\text{int}}$ , the thermodynamic stability of complexes has been explored. The simulated outcomes of all complexes lie in the range of efficient NLO material such as red-shifted  $\lambda_{\text{max}}$ , ameliorated  $\alpha_{\text{O}}$  and  $\beta_{\text{O}}$ , narrowed  $E_{\text{g}}$  and lowered  $E_{\text{opt}}$  of all doped complexes in comparison with pure GY and 2GY. Among molecular complexes of model 1; highest  $\lambda_{\text{max}}$  is exhibited by GY@3Ag<sub>center</sub> (536 nm) with the lowest  $E_{\text{opt}}$  of 2.31 eV among all molecular systems. The newly doped systems (GY@Ag<sub>center</sub>–GY@3Ag<sub>center</sub>) are enriched with a higher dipole moment  $\mu_{\text{e}}$  (0.385–3.873 D) in H<sub>2</sub>O than GY (0.001 D). Likewise, 2GY@3Ag<sub>center</sub> has highest  $\lambda_{\text{max}}$  of 548 nm, lowest  $E_{\text{opt}}$  of 2.31 eV and much narrower  $E_{\text{g}}$  of 2.55 eV in model 2 complexes (2GY@Ag<sub>center</sub>–2GY@3Ag<sub>center</sub>). Infrared (IR) and NCI analysis are performed to study the types of vibrations associated and nature of interaction. Higher values of electrical conductivities of all complexes resulted from strong dopant–surface interaction and efficient  $n \rightarrow \sigma^*$  charge transfer. All computationally computed parameters advocate the potential of using all doped complexes of model 1 as well as model 2 in integrated NLO devices and open new routes for designing highly efficient NLO materials. Moreover, more virtuous and upstanding outcomes have been revealed by complexes in which graphyne surface was comprised of two-unit cell. To sum up, the current research yields deep insight into tuneable NLO characteristics of Ag doped on graphyne surface.

## Author contributions

Saba Zahid: major contribution, the acquisition, drafting, analysis, writing original paper, working and interpretation of data.

Alvina Rasool: the acquisition, drafting, analysis, working, and interpretation of data.

Ali Raza Ayub: the acquisition, drafting, analysis, working, and interpretation of data.

Khurshid Ayub: the acquisition, drafting, analysis, working, and interpretation of data.

Javed Iqbal\*: substantial contribution to research design, the acquisition, analysis, and interpretation of data, and approval of the submitted and final version. M. S. Al-Buriahi: the acquisition, drafting, analysis, working, and interpretation of data. Norah Alwada'i: the acquisition, drafting, analysis, working, and interpretation of data. H. H. Somaily: the acquisition, drafting, analysis, working, and interpretation of data.

## Conflicts of interest

There are no declared conflicts.

## Acknowledgements

The authors thank the Punjab Bio-energy Institute (PBI), University of Agriculture (UAF), Faisalabad 38000, Pakistan, for financial and technical support. The authors express their gratitude to Princess Nourah bint Abdulrahman University Researchers Supporting Project (Grant No. PNURSP2022R11), Princess Nourah bint Abdulrahman University, Riyadh, Saudi

Arabia. This work was supported by King Khalid University through a grant (RCAMS/KKU/G001/21) under the Research Center for Advanced Materials Science (RCAMS) at King Khalid University, Saudi Arabia.

## References

- 1 A. Ahsin and K. Ayub, *Optik*, 2021, **227**, 166037.
- 2 O. Mhibik, S. Forget, D. Ott, G. Venus, I. Divliansky, L. Glebov and S. Chénais, *Light: Sci. Appl.*, 2016, **5**, e16026.
- 3 C. J. Brabec, *Sol. Energy Mater. Sol. Cells*, 2004, **83**, 273–292.
- 4 H. Hasegawa and T. Sato, *Electrochim. Acta*, 2005, **50**, 3015–3027.
- 5 C. Cheng, C. Zhu, B. Huang, H. Zhang, H. Zhang, R. Chen, W. Pei, Q. Chen and H. Chen, *Adv. Mater. Technol.*, 2019, **4**, 1800729.
- 6 J. M. Hales, M. Cozzuol, T. E. Screen, H. L. Anderson and J. W. Perry, *Opt Express*, 2009, **17**, 18478–18488.
- 7 S. Achelle, C. Baudequin and N. Plé, *Dyes Pigm.*, 2013, **98**, 575–600.
- 8 S. S. Varghese, S. Lonkar, K. Singh, S. Swaminathan and A. Abdala, *Sens. Actuators, B*, 2015, **218**, 160–183.
- 9 A. Karakas, A. Elmali and H. Unver, *Spectrochim. Acta, Part A*, 2007, **68**, 567–572.
- 10 R. Baloach, K. Ayub, T. Mahmood, A. Asif, S. Tabassum and M. A. Gilani, *J. Inorg. Organomet. Polym. Mater.*, 2021, **31**, 3062–3076.
- 11 M. Ishaq, R. A. Shehzad, M. Yaseen, S. Iqbal, K. Ayub and J. Iqbal, *J. Mol. Model.*, 2021, **27**, 1–11.
- 12 S. Muhammad, M. R. S. A. Janjua and Z. Su, *J. Phys. Chem. C*, 2009, **113**, 12551–12557.
- 13 R. A. Shehzad, S. Muhammad, J. Iqbal, A. G. Al-Sehemi, M. Yaseen, Z. Aloui and M. Khalid, *J. Mol. Model.*, 2021, **27**, 1–10.
- 14 A. U. Khan, S. Muhammad, R. A. Khera, R. A. Shehzad, K. Ayub and J. Iqbal, *Optik*, 2021, **231**, 166464.
- 15 A. Irfan, M. Pannipara, A. G. Al-Sehemi, M. W. Mumtaz, M. A. Assiri, A. R. Chaudhry and S. Muhammad, *Z. Phys. Chem. (Muenchen, Ger.)*, 2019, **233**, 1625–1644.
- 16 D. Xiao, F. A. Bulat, W. Yang and D. N. Beratan, *Nano Lett.*, 2008, **8**, 2814–2818.
- 17 L. Zhu, K. Xue and J. Hou, *J. Mol. Model.*, 2019, **25**, 1–10.
- 18 M. J. Lee, M. Piao, M.-Y. Jeong, S. H. Lee, K. M. Kang, S.-J. Jeon, T. G. Lim and B. R. Cho, *J. Mater. Chem.*, 2003, **13**, 1030–1037.
- 19 Y.-D. Song and Q.-T. Wang, *Optik*, 2020, **220**, 164947.
- 20 R. Baughman, H. Eckhardt and M. Kertesz, *J. Chem. Phys.*, 1987, **87**, 6687–6699.
- 21 X. Li and S. Li, *J. Mater. Chem. C*, 2019, **7**, 1630–1640.
- 22 M. Zhang, X. Wang, H. Sun, J. Yu, N. Wang, Y. Long and C. Huang, *2D Materials*, 2018, **5**, 035039.
- 23 A. Bhaskar, R. Guda, M. M. Haley and T. Goodson III, *J. Am. Chem. Soc.*, 2006, **128**, 13972–13973.
- 24 K. Srinivasu and S. K. Ghosh, *J. Phys. Chem. C*, 2012, **116**, 5951–5956.
- 25 H. Zhang, X. Zhao, M. Zhang, Y. Luo, G. Li and M. Zhao, *J. Phys. D: Appl. Phys.*, 2013, **46**, 495307.



- 26 M. Frisch, G. Trucks, H. Schlegel, G. Scuseria, M. Robb, J. Cheeseman, G. Scalmani, V. Barone, B. Mennucci and G. Petersson, *Google Scholar There is no corresponding record for this reference*, 2015.
- 27 T. Yanai, D. P. Tew and N. C. Handy, *Chem. Phys. Lett.*, 2004, **393**, 51–57.
- 28 A. Klamt, C. Moya and J. Palomar, *J. Chem. Theory Comput.*, 2015, **11**, 4220–4225.
- 29 S. Gorelsky, *A Library for Package-Independent Computational Chemistry Algorithms*, University of Ottawa, Ottawa, Canada, 2010.
- 30 A. S. Rad and K. Ayub, *J. Alloys Compd.*, 2016, **672**, 161–169.
- 31 R. A. Shehzad, J. Iqbal, K. Ayub, F. Nawaz, S. Muhammad, A. R. Ayub and S. Iqbal, *Optik*, 2021, **226**, 165923.
- 32 N. M. O'boyle, A. L. Tenderholt and K. M. Langner, *J. Comput. Chem.*, 2008, **29**, 839–845.
- 33 T. Lu and F. Chen, *J. Comput. Chem.*, 2012, **33**, 580–592.
- 34 M. R. S. A. Janjua, C.-G. Liu, W. Guan, J. Zhuang, S. Muhammad, L.-K. Yan and Z.-M. Su, *J. Phys. Chem. A*, 2009, **113**, 3576–3587.
- 35 M. R. S. A. Janjua, Z. H. Yamani, S. Jamil, A. Mahmood, I. Ahmad, M. Haroon, M. H. Tahir, Z. Yang and S. Pan, *Aust. J. Chem.*, 2015, **69**, 467–472.
- 36 S. Zahid, A. Rasool, M. Ans, M. Yaseen and J. Iqbal, *Energy Fuels*, 2021, **35**, 15018–15032.
- 37 A. Rasool, S. Zahid, R. A. Shehzad, M. S. Akhter and J. Iqbal, *Comput. Theor. Chem.*, 2021, **1203**, 113359.
- 38 A. U. Khan, R. A. Khera, N. Anjum, R. A. Shehzad, S. Iqbal, K. Ayub and J. Iqbal, *RSC Adv.*, 2021, **11**, 7779–7789.
- 39 F. Ullah, N. Kosar, K. Ayub, M. A. Gilani and T. Mahmood, *New J. Chem.*, 2019, **43**, 5727–5736.
- 40 S. Zahid, A. Rasool, M. Ans, M. Salim Akhter, J. Iqbal, M. S. Al-Buriahi, S. Alomairy and Z. A. Alrowaili, *Sol. Energy*, 2022, **231**, 793–808.
- 41 A. Rasool, S. Zahid, M. Ans, J. Iqbal, M. Adnan, E.-S. M. Sherif and M. S. Al-Buriahi, *Opt. Mater.*, 2022, **123**, 111907.
- 42 R. Habibpour and R. Vaziri, *Int. J. Nano Dimens.*, 2016, **7**, 208–224.
- 43 G. Landi, H. C. Neitzert, C. Barone, C. Mauro, F. Lang, S. Albrecht, B. Rech and S. Pagano, *Adv. Sci.*, 2017, **4**, 1700183.
- 44 F. Ullah, N. Kosar, M. N. Arshad, M. A. Gilani, K. Ayub and T. Mahmood, *Opt Laser. Technol.*, 2020, **122**, 105855.
- 45 H. H. Cho, S. Kim, T. Kim, V. G. Sree, S. H. Jin, F. S. Kim and B. J. Kim, *Adv. Energy Mater.*, 2018, **8**, 1701436.
- 46 F. Manzoor, J. Iqbal, Z. Zara, B. Eliasson, M. S. Mahr and K. Ayub, *ChemistrySelect*, 2018, **3**, 1593–1601.
- 47 S. Zahid, A. Rasool, R. A. Shehzad, I. A. Bhatti and J. Iqbal, *J. Mol. Model.*, 2021, **27**, 1–14.
- 48 A. Rasool, S. Zahid, M. Ans, S. Muhammad, K. Ayub and J. Iqbal, *ACS Omega*, 2021, **7**, 844–862.
- 49 M. U. Khan, M. Ibrahim, M. Khalid, S. Jamil, A. A. Al-Saadi and M. R. S. A. Janjua, *Chem. Phys. Lett.*, 2019, **719**, 59–66.
- 50 S. Iyasamy, K. Varadharajan and S. Sivagnanam, *Z. Phys. Chem. (Muenchen, Ger.)*, 2016, **230**, 1681–1710.
- 51 M. Drissi, N. Benhalima, Y. Megrouss, R. Rachida, A. Chouaih and F. Hamzaoui, *Molecules*, 2015, **20**, 4042–4054.
- 52 R. Kiran, R. A. Khera, A. U. Khan, A. Ayoub, N. Iqbal, K. Ayub and J. Iqbal, *J. Mol. Struct.*, 2021, **1236**, 130348.
- 53 I. Munir, M. Perveen, S. Nazir, R. A. Khera, A. R. Ayub, K. Ayub and J. Iqbal, *J. Mol. Liq.*, 2021, **336**, 116327.
- 54 M. D. Mohammadi, 2021.
- 55 M. D. Mohammadi and H. Y. Abdullah, *J. Mol. Model.*, 2020, **26**, 1–15.
- 56 X. Li and J. Lu, *Phys. Chem. Chem. Phys.*, 2019, **21**, 13165–13175.
- 57 L. Ma, J.-M. Zhang, K.-W. Xu and V. Ji, *Appl. Surf. Sci.*, 2015, **343**, 121–127.

